ROR2 drives right ventricular heart failure via disruption of proteostasis

Hali Hartman B.S.[1], Genevieve Uy B.S.[1], Keita Uchida Ph.D.[2], Emily A. Scarborough Ph.D.[2], Yifan Yang M.S.[3], Eric Barr B.S.[1,3], Spencer Williams B.S.[1], Sanam L. Kavar B.S.i[3], Jeff Brandimarto M.S.[3], Li Li B.S.[2], Ling Lai M.D.[3], Joanna Griffin[3], Nora Yucel Ph.D.[3], Swapnil Shewale Ph.D.[3], Hari Rajagopal[1], Deborah M. Eaton Ph.D.[3], Tanis Dorwart B.S.[4], Kenneth C. Bedi Jr B.S.[3], Crystal S. Conn Ph.D.[4], Kenneth Margulies M.D.[3], Benjamin Prosser Ph.D.[2], Zoltan Arany M.D., Ph.D.[3], Jonathan J. Edwards M.D.[1,3]

[1]Cardiovascular Institute, Children's Hospital of Philadelphia, Philadelphia, PA, USA

[2]Department of Physiology, Pennsylvania Muscle Institute, Perelman School of Medicine, University of Pennsylvania, Philadelphia, PA, USA

[3]Cardiovascular Institute, Perelman School of Medicine, University of Pennsylvania, Philadelphia, PA, USA

[4]Department of Radiation Oncology, Perelman School of Medicine, University of Pennsylvania, Philadelphia, PA, USA

Short Title: ROR2 drives right ventricular heart failure

Correspondence to:

Jonathan Edwards, MD

University of Pennsylvania

Cardiovascular Institute

3401 Civic Center Blvd

Smilow Center for Translational Research, Room 11-114

Philadelphia, PA 19104

EdwardsJ6@chop.edu

Zoltan Arany, MD, PhD
University of Pennsylvania
Cardiovascular Institute
3401 Civic Center Blvd
Smilow Center for Translational Research, Room 11-106
Philadelphia, PA 19104
zarany@pennmedicine.upenn.edu
Word Count: 4386

Abstract

Background: No therapies exist to reverse right ventricular failure (RVF), and the molecular mechanisms that drive RVF remain poorly studied. We recently reported that the developmentally restricted noncanonical WNT receptor ROR2 is upregulated in human RVF in proportion to severity of disease. Here we test mechanistic role of ROR2 in RVF pathogenesis.

Methods: ROR2 was overexpressed or knocked down in neonatal rat ventricular myocytes (NRVMs). ROR2-modified NRVMs were characterized using confocal microscopy, RNAseq, proteomics, proteostatic functional assays, and contractile properties with pacing. The impact of cardiac ROR2 expression was evaluated in mice by AAV9-mediated overexpression and by AAV9-mediated delivery of shRNA to knockdown ROR2 in a pulmonary artery banded pressure overload RVF model. ROR2-modified mice were evaluated by echocardiography, RV protein synthetic rates and proteasome activity.

Results: In NRVMs, we find that ROR2 profoundly dysregulates the coordination between protein translation and folding. This imbalance leads to excess protein clearance by the ubiquitin proteasome system (UPS) with dramatic impacts on sarcomere and cytoskeletal structure and function. In mice, forced cardiac ROR2 expression is sufficient to disrupt proteostasis and drive RVF, while conversely ROR2 knockdown partially rescues proteostasis and cardiac function in a pressure overload model of RVF.

Conclusions: In sum, ROR2 is a key driver of RVF pathogenesis through proteostatic disruption and, thus, provides a promising target to treat RVF.

Introduction

Right ventricular failure (RVF) is a widespread problem for which there are no proven therapies. Nearly half of patients with left ventricular failure (LVF) develop RVF, and RVF doubles their risk of death.[1,2] RVF is also the leading cause of hospital admission and death in pulmonary hypertension.[3-5] Several therapies reduce morbidity and mortality in patients with LVF, but none of these therapies have proven efficacious for patients with RVF, and in fact some even lead to worse outcomes.[6-12] RVF thus fundamentally differs from LVF, and finding new therapies for RVF will require a better understanding of the unique molecular drivers of RVF.

Recently, we leveraged a large cohort of post-transplant hearts from patients with dilated or ischemic cardiomyopathy to discover that the noncanonical WNT receptor ROR2, which is usually restricted to the developing heart, is robustly upregulated in failing RVs in correlation with the severity of RVF.[13] ROR2 is critical to cardiac development, with *Ror2* knockout mice developing ventricular septal defects.[14] Although *Ror1* knockout mice have no cardiac defects, its loss is additive such that *Ror1/Ror2* double knockout causes more severe phenotypes including complex conotruncal defects and ventricular noncompaction.[14-16] However, the mechanistic role of ROR2 in RVF has not been studied. Therefore, we set out to test if and how ROR2 induction causes RVF and uncover a previously unrecognized role for ROR2 in regulating cardiomyocyte proteostasis. We find that ROR2 activates protein translation while simultaneously reducing expression of HSP70, a critical protein chaperone. Thus, protein production is increased and protein folding is compromised. Ultimately, the increased proteasome-mediated clearance is either not sufficient or excessive to the point of being counterproductive resulting in RV dilation and dysfunction. Importantly preventing the ROR2 induction in a mouse model of RVF ameliorated both cardiac proteostatic disruption and RVF.

Taken together, we propose that targeting ROR2-driven proteostatic disruption may serve as a novel therapeutic strategy to treat RVF.

Methods

Detailed methods are provided in the Supplemental Material. Source data supporting the findings and displayed in main figures and supplemental figures are included in source data. RNAsequencing data generated for this study was deposited in the Gene Expression Omnibus under the accession number GSE278627. The mass spectrometry proteomics data have been deposited to the ProteomeXchange Consortium via the PRIDE partner repository with the dataset identifier PXD05655.

Animal Studies

All animal work was performed under University of Pennsylvania Institutional Animal Care and Use Committee approved protocols (#805255 and #805309). Neonatal rat ventricular myocytes (NRVMs) were isolated from 1-2 day old Sprague Dawley rats after obtaining pregnant rats from Charles River Laboratory and maintained in culture as previously described.[17] C57BL6 mice obtained from Jackson Laboratory were used for all mouse experiments studies.

Human Studies

Procurement of all human RV myocardial tissue was performed in accordance with protocols approved by the University of Pennsylvania Institutional Review Board (approval 802781) and the Gift-of-Life Donor Program, Philadelphia, PA. Prospective informed consent for research use of surgically explanted tissue was obtained from the transplant recipients or from the next-of-kin in the case of deceased organ donors, as previously described.[18]

Statistical Analyses

RNAseq and proteomics data were analyzed in RStudio using the voom function from the Limma package (version 3.56.1) to transform and normalize the data, and the toptable function to output the differential analysis result. Two group and three group statistical comparisons were performed using T-test/Mann Whitney U or One-Way ANOVA/Kruskal-Wallis based on normality in GraphPad Prism v10.

Results

Cardiomyocyte ROR2 expression is developmentally restricted and reactivated in RV failure

ROR2 is known to be involved in cardiac development, but its expression is broadly absent in healthy adult tissues.[19] The temporal cadence for this natural suppression of ROR2 in the heart and its histologic expression pattern in the heart has not been well characterized. By qPCR and western blot we observe that about 90% of ventricular myocardial ROR2 is lost in mice from P2 to P7 and is nearly extinguished by P21 (**Fig. 1a, Supplementary Fig. 2a/b**). On histology, myocardial ROR2 at birth is observed predominantly in cardiomyocytes, and localizes to the cell membrane and nucleus (**Fig 1b** and **Supplementary Fig. 2c**). As the expression tapers, ROR2 is minimally retained and mostly observed in the atria and subepicardium (**Fig 1a** and **Supplementary Fig. 2c/d**), consistent with prior single nuclear RNAseq datasets.[20,21]

We previously found that ROR2 is re-expressed in human RVF in a severity dependent manner, localizing to both cardiomyocytes and fibroblasts.[13] Since this pattern differs from reports in mouse LVF in the context of transverse aortic constriction, in which ROR2 is restricted to non-cardiomyocytes, we first tested if and where ROR2 is reactivated in the failing RV in mice.[22] To that end, we used a pulmonary artery banding (PAB) pressure overload model to generate RVF. With an average pressure gradient of ~60-70mmHg, PAB mice developed clear markers of pathologic RV remodeling and RVF with increased RV mass and echocardiographic increases in RV wall thickness, RV dilation, systolic dysfunction, and tricuspid insufficiency (**Fig. 1c-f** and **Supplementary Table 4**). By histology, PAB demonstrated RV hypertrophy and diffuse RV fibrosis (**Fig. 1g**). PAB RVs also increased expression of the fetal myosin heavy chain gene MYH7 and the natriuretic peptide gene *Nppb*, both known markers of heart failure **(Fig. 1h/i**). Since we observed early postnatal ROR2 expression localizing to the cell membrane and the nucleus, we assessed ROR2 expression using a method that separates proteins into a cytoplasmic fraction that is depleted of nuclear and cytoskeleton proteins ("NCD") using a Triton-based buffer and a separate fraction that is enriched for nuclear and cytoskeleton proteins ("NCE") using a thiourea based buffer (**Supplementary Fig. 1b/c**). Most ROR2 localized to the NCD fraction, in which PAB mice demonstrated a 5-fold increase. Notably, ROR2 was essentially absent from the NCE fraction in sham mice, where PAB mice demonstrated a greater than 35-fold increase (**Fig. 1j/k**). Thus, the normally developmentally restricted ROR2 is robustly reexpressed in mouse RVF (**Fig 1l**). Moreover, NCE ROR2 correlated to RV functional and structural changes in PAB including RV dilation (r=0.66), TAPSE (r= -0.68), and fractional area change (r= -0.60) ($p<0.05$ for all, **Supplementary Table 4**). In contrast, NCD ROR2 did not correlate well to any of these RV functional or structural parameters. By immunohistochemistry and RNAscope, ROR2 was expressed by both cardiomyocytes and fibroblasts in the PAB RV. ROR2 protein in cardiomyocytes frequently localized to the nucleus (**Fig. 1m**) similar to ~P2-P7 mouse RV and consistent with the

NCD/NCE fractionation. This was also consistent with our previous findings in human RVF immunohistochemistry and further supported by complementary RNAscope from human RV in this study (**Supplementary Fig. 2e).** We conclude that ROR2 expression, especially NCE ROR2, is strongly induced during RVF in mice and in proportion to RVF severity.

ROR2 regulates cardiomyocyte morphology and function

Since little is known about the role of ROR2 in cardiomyocytes, we directly tested the impact of induction and loss of ROR2 using NRVMs. We cultured cells on patterned substrates to promote sarcomere alignment and enhance structural characterization. Using adenovirus, we overexpressed human ROR2 ($ROR2^{OE}$) or knocked down native *Ror2* by shRNA ($ROR2^{KD}$) using GFP as a reporter (**Fig. 2a/b**). Adeno-GFP alone was used as a control. $ROR2^{OE}$ and $ROR2^{KD}$ caused dichotomous morphologic changes. $ROR2^{OE}$ NRVMs were significantly smaller, driven by reduction in the longitudinal major axis resulting in a rounded appearance and smaller aspect ratio of the major to the minor axis, with fragmented appearing sarcomeres (**Fig. 2c-e**). In contrast, $ROR2^{KD}$ NRVMs were slightly larger without affecting the aspect ratio. We also observed opposing effects on cell-cell junctions with the intercalated disc (ICD) proteins α-actinin, β-catenin, and Cx43 being enriched in the cellular periphery in $ROR2^{KD}$ and largely lost in $ROR2^{OE}$ (**Fig. 2f-h** and **Supplementary Fig. 3a**). Total staining intensity and protein expression by western blot for Cx43 and α-actinin increased in $ROR2^{OE}$ NRVMs, while β-catenin levels were stable, indicating that reduced peripheral staining represents redistribution of the proteins rather than loss (**Fig 2i-l)**. Thus, ROR2 regulates gross cardiomyocyte morphology and both abundance and localization of ICD/adhesion proteins.

We next tested the impact of ROR2 modulation on cardiomyocyte contractile function. Using an IonOptix Cytocypher pacing apparatus, we found that ROR2^{OE} and ROR2^{KD} had significant and opposite effects on NRVM relaxation kinetics with ROR2^{OE} significantly slowing and ROR2^{KD} significantly accelerating relaxation (**Fig. 2m-p**).

ROR2 regulates cardiomyocyte proteostasis by affecting the ubiquitin-proteasome system, protein synthesis, and folding

To explore potential mechanisms to explain these NRVM structural phenotypes, we performed RNAseq of ROR2^{OE} and ROR2^{KD} NRVMs (**Fig. 3a** and Supplementary Data 4). We observed no significant changes in known β-catenin responsive transcriptional targets between ROR2^{OE} and ROR2^{KD} NRVMs, suggesting that these structural phenotypes were not the result of modulating canonical Wnt signaling (**Supplementary Table 5**). Instead, gene-set enrichment analysis revealed changes in protein turnover gene programs with upregulation in genes associated with ubiquitin ligase activity and downregulation for ubiquitin-dependent protein catabolism in ROR2^{OE} compared to ROR2^{KD} NRVMs (**Fig. 3b**). Although not reaching statistical significance, the two HSP70 paralogs *Hspa1a* and *Hspa1b* (adj p =0.059, both) exhibited the highest magnitude reduction in ROR2^{OE}. Multiple other chaperones were also trending as significantly downregulated (adj p <0.1) including *Hsph1*, *Hsp90aa1/ab1*, *Dnajb1/a1*, *Hspa4,* and *Cryab* (**Fig 3a)**.

These data suggested that dysregulated ROR2 has important effects on protein homeostasis. Consistent with this notion, western blots revealed a striking reduction in total ubiquitinated proteins in ROR2^{OE} NRVMs, while conversely increased in ROR2^{KD} NRVMs, paralleling HSP70 expression (**Fig. 3c-e**). The other tested chaperones were frequently increased in ROR2^{KD}

NRVMs but unchanged or trending towards an increase in ROR2^{OE} NRVMs (**Supplementary Fig. 3b**). To test whether the reduction of ubiquitinated proteins in ROR2^{OE} NRVMs was driven by increased turnover or by a decrease in ubiquitination, we repeated these experiments with the addition of the competitive proteasome inhibitor MG132, thus blocking clearance of ubiquitinated proteins. Under these conditions, proteasome-directing K48-linked ubiquitination (but not autophagy directing K63-linked or total ubiquitination) increased significantly more in the ROR2^{OE} compared to the other groups (**Fig. 3f/g** and **Supplementary Fig. 3c/d**). Interestingly, the pattern of total ubiquitin accumulation after MG132 differed between ROR2^{OE} and ROR2^{KD} NRVMs, with high molecular weights (> ~150kDa) more robustly increased in ROR2^{OE} and low molecular weights (<~60 kDa) preferentially increased in ROR2^{KD} NRVMs (**Supplementary Fig. 3d**), suggesting that ROR2 may selectively impact the synthesis and/or turnover of certain groups of proteins. To directly measure the impact of ROR2 expression on UPS activity, we measured maximal proteasome capacity from NRVM lysates using the chymotrypsin-like substrate peptide and fluorescent reporter Suc-LLVY-AMC. Expression of the chymotrypsin-like proteasome subunit (Psmb5) did not change significantly in ROR2^{OE} or ROR2^{KD} cells, but its activity was significantly decreased in ROR2^{KD}, in either absence or presence of ATP supplementation (**Fig. 3h**), suggesting mechanisms other than relative proteasome abundance drive ROR2-responsive UPS turnover rates. We conclude that ROR2 has graded effects on UPS activity, whereby high expression of ROR2 increases UPS flux without altering its maximal capacity, while conversely low expression of ROR2 decreases maximal proteasome capacity.

Given that proteasome-mediated clearance appears to be increased in ROR2^{OE} NRVMs without directly increasing maximal proteasome capacity, we tested whether other factors involved in protein production and stability may also be disrupted. We quantified global protein translation

rates by using the tyrosyl tRNA analogue puromycin and radiolabeled ^{35}S-Met to label newly synthesized proteins. By puromycin labeling, ROR2^{OE} resulted in ~3-fold increase in newly synthesized proteins with a modest decrease in translation rate in the ROR2^{KD} (**Fig. 3i)**. ^{35}S-Met labeling revealed similar results with ~1.5-fold increase in ROR2^{OE} and ~0.6 fold reduction in ROR2^{KD} (**Fig. 3j**). These data indicate that ROR2 expression, in addition to promoting UPS flux, also promotes global protein synthesis in NRVMs.

Differences in chaperone expression were unlikely to account for these ROR2-driven effects on protein synthesis, because HSP70 overexpression (HSP70^{OE}) did not reverse the enhanced translation rates in ROR2^{OE} (**Fig 3k**). On the other hand, HSP70^{OE} did increase ubiquitin levels, suggesting that restoring HSP70 decreased UPS turnover in ROR2^{OE} (**Fig 3l)**. We suspected that HSP70 does so by improving protein folding and quality, based in part on the observation that ROR2^{OE} NRVMs with a GFP reporter had diminished GFP fluorescence, which is dependent on proper folding, and which could be rescued by HSP70^{OE} without substantially changing total GFP protein levels (**Supplementary Fig. 4c-f**). To measure protein folding capacity directly, we used a luciferase refolding assay in which heat-shocked recombinant pLuc is allowed to refold in cell lysates and interrogated by its ability to cleave luciferin and generate light (**Fig. 3m**). Heat-shocked recombinant pLuc had strongly impaired ability to refold and cleave luciferin in ROR2^{OE} compared to ROR2^{KD} lysates. Taken together, these data show that ROR2 profoundly disrupts cardiomyocyte proteostasis by promoting protein translation while simultaneously suppressing proper protein folding capacity, priming NRVMs to clear these misfolded proteins through the UPS.

ROR2 regulates cardiomyocyte proteome

In light of the profound effects of ROR2 on translation and proteasome-clearance of misfolded proteins, we next sought to characterize in an unbiased fashion how ROR2 expression impacts the global proteome. $ROR2^{OE}$ in NRVMs had profound effects on the proteome, an effect partly mitigated by proteasomal inhibition (**Fig. 4a-c**). Few proteasome subunits were affected, in keeping with $ROR2^{OE}$ NRVMs having similar Psmb5 expression, as noted above. In contrast, we noted 20 upregulated and 26 downregulated E3 ubiquitin ligases in $ROR2^{OE}$ cells—some of which was reversed by proteasome inhibition—indicating substantial protein substrate-specificity for ROR2-driven UPS-mediated clearance (**Fig**. **4d/e**, Supplementary Data 20 and 21). These included upregulation of OZZ-E3 (*Neurl2*)—a ubiquitin ligase that specifically targets the intercalated disc pool of β-catenin—and ITCH—which targets the non-canonical WNT signaling protein DVL (**Fig 4d**)**.** PDZRN3, an E3 ligase that was recently identified as a likely indirect ROR2 phosphorylation target and which plays a role in postnatal sarcomerogenesis and ICD formation, was also significantly reduced. In contrast, no changes were observed for the components of the E3 ligase complex $SCF^{\beta\text{-}TRCP}$ that targets the transcriptional pool of β-catenin and is consistent with the above RNAseq findings that demonstrated no substantial changes in canonical WNT signaling. Pathway enrichment analysis of upregulated differentially expressed proteins in $ROR2^{OE}$ NRVMs revealed enrichment of multiple biological processes including triglyceride biosynthesis, extracellular matrix proteins, integrin-mediated signaling, heart contraction, and response to insulin. Downregulated proteins were enriched for regulation of proline hydroxylation, sarcomere and actin filament organization, supramolecular organization, and inhibitors of apoptosis (**Fig. 4f**). Downregulation of actin/sarcomere associated proteins was broadly reversed after MG132 including: TPM1/2/3, XIRP1/2, MYOZ2, LMOD2, FLNC, NRAP, and TNT2 (**Fig. 4g**).

Cardiac ROR2 expression causes right ventricular failure and proteostatic disruption

Given the marked effects of ROR2^{OE} in cardiomyocytes in cell culture, we next sought to test the effect of ROR2 expression in the RV *in vivo*. To this end, we generated cardiac ROR2^{OE} mice using AAV9 to deliver HA-tagged ROR2 versus GFP in 4-week-old male and female mice (**Fig. 5a**). At 8 weeks after injection, we observed robust RV and LV ROR2 expression, which localized appropriately to the cardiomyocyte membrane in contrast to the diffuse staining for GFP (**Fig. 5b**). ROR2^{OE} led to significant and predominantly RV cardiac hypertrophy in male mice, marked by an increase in RV wall area, RV mass, and RV cardiomyocyte cross-sectional area by minimum Feret Diameter (**Fig. 5b-h**). Echocardiography (n=8/group, 50% male) revealed biventricular dilation and systolic dysfunction in male ROR2^{OE} mice (**Fig. 5i-l**). Intravenous catheterization revealed male-specific increase in RV end diastolic pressure (**Fig. 5m**). ROR2^{OE} mice also exhibited induction of *Nppb* mRNA and fetal MYH7 **(Fig. 5n/o**) without causing an increase in fibrosis (**Fig. 5p**). The cardiac dysfunction seen in male ROR2^{OE} mice was accompanied by proteostatic disruptions similar to those seen in NRVMs, i.e. lower *Hspa1b* mRNA expression, decreased cardiomyocyte ubiquitin staining, increased protein translation, and increased proteasome activity **(Fig. 5q-u**), as well as reduced peripheral β-catenin in RV cardiomyocytes. We conclude that ROR2 expression is sufficient to drive cardiac failure *in vivo* in male mice, concomitant with disruption of proteostasis. Female ROR2^{OE} mice were generally much less affected.

Suppression of ROR2 induction in RV pressure overload abrogates RV failure and proteostatic disruption

The results above demonstrated that ROR2 expression was sufficient to cause RV dysfunction and disrupt proteostasis. We next sought to test if ROR2 expression was necessary for the development of RV dysfunction in the PAB mouse model. We first evaluated the impact of PAB on cardiac proteostatic processes, noting that PAB increased RV protein translation, HSP70 expression, proteasome capacity, and total polyubiquitin (particularly in the NCD fraction) without an increase in UPS-directing K48-linked ubiquitin (**Fig. 6a-g**). Thus, the mouse PAB RVF model demonstrates clear proteostatic disruption with an increase in both protein translation and UPS-mediated turnover, to some extent analogous to that found with $ROR2^{OE}$. Next, to determine if ROR2 induction in PAB contributes to RVF and proteostatic disruption, we injected mice with AAV9 to deliver *shRor2* (PAB^{shRor2}, n = 15) or scrambled shRNA (PAB^{shScr}, n=15) prior to PAB (**6h**). PAB^{shRor2} had ~25% lower NCD and ~50% lower NCE ROR2 in the RV (**Fig. 6i/j**). Strikingly, PAB^{shRor2} mice demonstrated less severe RV dilation, decreased incidence of tricuspid insufficiency, better RV systolic function measured by TAPSE (**Fig. 6j-l**), improved diastolic function (**Fig. 6m**), less RV fibrosis, and reduction in RV wall area by histology (**Fig. 6k-p**). ROR2 knockdown also improved the proteostatic dysfunction in PAB with decreases in protein translation rates, HSP70 induction, and K48-linked ubiquitin without affecting proteasome activity capacity (**Fig. 6q-t**), partially reversing the PAB-induced defects. Taken together, these data demonstrate that ROR2 knockdown protects from pathologic RV remodeling and improves RV function in response to pressure overload, concomitant with partial reversion of the proteostasis disruption.

ROR2 Expression in Human RVF Correlates to Proteasome Activity

Finally, we determined the relationship between ROR2 expression and markers of proteostasis in human RVF. To do so, we leveraged a collection of post-transplant hearts from patients with

DCM, compared to non-failing hearts from organ donors. The DCM hearts were stratified by whether they also exhibited RVF versus pRV, and the RVF hearts were further stratified by whether they exhibited high or low ROR2 expression (**Fig 7a**). Proteasome capacity was robustly increased in high ROR2-expressing RVF, especially at low ATP concentrations, which may indicate preferential activity of the ATP-independent 20S proteasome that is known to be upregulated in heart failure ($p < 0.0001$ for two-way ANOVA; **Fig. 7b**).[23] ROR2 expression levels in the NCE fraction in RVF correlated tightly with proteasome activity across a range of ATP concentrations ($r = 0.744 – 0.964$, $p < 0.05$; **Fig. 7c** and Supplementary Table 11). The expression of the catalytically active proteasome domain PSMB5 was only mildly affected in high ROR2-RVF and total ubiquitin levels were unchanged. We conclude that in human cardiomyopathy, as in mice, high ROR2 expression—particularly in the NCE fraction—is associated with RVF and with proteostatic disruption.

Discussion

RVF is widespread and remains a challenging problem for which there are no proven therapies. Using standard LVF medications to treat RVF has not shown clear benefit, indicating the presence of distinct RVF mechanisms.[6-12,24] In severe human RVF, we found that the developmentally restricted noncanonical WNT receptor ROR2 is pathologically reactivated by both cardiomyocytes and fibroblasts.[13] This expression pattern was also recapitulated in mouse RV pressure overload RVF and contrasts with a prior report in mouse LVF where ROR2 is restricted to noncardiomyocytes.[22] Here using a combination of in vitro and in vivo models as well as human cardiomyopathy biospecimens, we revealed a previously unrecognized role of

ROR2 in regulating cardiomyocyte proteostasis and contractile function. Our data point to a model wherein ROR2 promotes protein synthesis while simultaneously reducing folding capacity (**Fig. 7d**). Although UPS-mediated clearance is upregulated in this setting, this is either not sufficient to meet the demands or, potentially, chronically maladaptive and ultimately converges on a cardiomyocyte functional compromise. Thus, we propose that addressing ROR2-mediated proteostatic disruption represents a potential novel therapeutic avenue for RVF, for which no specific therapies currently exist.

ROR2 is a noncanonical cell surface WNT receptor without true kinase activity (i.e. a pseudokinase).[25] The downstream effects of ROR2 activation remain incompletely characterized but include at least three broad pathways: alterations in cell polarity via RAC/RHO, activation of a JNK/cJUN phosphorylation cascade, and activation of Ca^{2+}-responsive targets (e.g. PKC, CAMKII) via increases in intracellular Ca^{2+}.[26] The molecular and functional impact of pathogenic ROR2 expression has been mostly studied in the context of cancer, which has revealed that ROR2 induction causes context-specific pleiotropic phenotypes including evidence for both reduction and amplification of cancer cell death, invasiveness, and metastasis resulting in both positive and negative associations with patient mortality.[27,28] Previously, there were a few known connections linking ROR2-specifically or noncanonical WNT signaling generally to proteostasis. In cultured ovarian carcinoma cells that typically have low ROR2 expression, adenoviral delivery of ROR2 activated the unfolded protein response and caused apoptosis.[29] In kind, suppressing the induction of the endoplasmic reticulum stress protein IRE1a in this model could also rescue ROR2-mediated apoptosis, implicating proteostatic disruption as a key mediator of ROR2-induced cancer cell death. In cultured NRVMs, addition of ROR2's only known ligand—WNT5A—was shown to promote protein synthesis and drive cardiomyocyte hypertrophy.[30,31] These WNT5A effects could be blocked by

preventing the membrane localization of the ROR2 binding partner VANGL2 or by inhibiting JNK. In contrast to mTOR and ERK signaling, there is a paucity of evidence directly implicating JNK/cJUN in regulating protein synthesis. However, there is substantial evidence for crosstalk between WNT signaling with ERK and mTOR. For example, both canonical and noncanonical WNT activation can inhibit GSK3 through phosphorylation.[32,33] When active, GSK3 can phosphorylate a diverse and growing list of target proteins including the well-described canonical WNT signaling hub β-catenin and the mTOR regulatory and target proteins TSC2 and Raptor which results in inhibition and activation of mTORC1 signaling, respectively.[34-36] Likewise, in HEK293 cells, JNK has also been shown to activate mTORC1 via Raptor phosphorylation in response to osmotic stress.[37] In the context of ERK signaling, in A375 melanoma cells that typically have low ROR2 expression, induction of ROR2 caused ERK hyperactivation and cell death.[27] Moreover, in isolated mouse cardiomyocytes ERK1/2 activation and HSP70 expression demonstrate a reciprocally antagonistic relationship, with HSP70 knockdown being sufficient to cause contractile and relaxation deficits similar to what we observed with $ROR2^{OE}$ NRVMs.[38] Thus, ROR2 induction in cardiomyocytes could lead to pathologic translational hyperactivation via secondary activation of mTOR or ERK signaling by first modulating the activities of other true kinases such as JNK/cJUN or GSK3, ultimately leading to proteostatic disruption.

Upregulation of ROR2 in RVF fits within the well-recognized paradigm of fetal gene program reactivation during heart failure—some of which could be initially adaptive.[39,40] For example, to accommodate hypertrophic growth during initial cardiac remodeling, similar to the proliferative state of cardiac development, there is a need to amplify protein production.[41,42] A physiologic or adaptive activation of a translational program should be accompanied by an equally matched enhancement of protein folding capacity. In keeping with this, during human heart development

ROR2 and *HSPA1A/B* mRNA levels are positively correlated with higher levels at more immature stages.[43] Likewise, we found that during postnatal cardiac maturation a reduction in HSP70 occurred only after ROR2 downregulation. With mouse PAB, the RV increases all three components: translation, folding capacity, and proteasome activity. Since ubiquitin still accumulates in the PAB RV, it suggests the increase in these three components is imbalanced favoring excess translation.[42] Furthermore, since knockdown of ROR2 in PAB improves RV remodeling and function and most prominently affects protein synthesis rates, it suggests that abating some of the translational hyperactivation may be the critical factor to restore proteostatic balance in RVF.

Cardiomyocytes are particularly vulnerable to proteostatic disruption in that they are dependent on maintaining a high quality pool of contractile elements including large proteins (e.g. Titin, Myosin) that suffer wear and tear during cardiac cycles.[44] Paradoxically though, cardiomyocytes exhibit natural strategies to slow translation with ongoing maturation.[45] A potential teleological explanation for this is that the upfront energy investment incurred by slowing translation is ultimately offset by improved accuracy and, therefore, quality of sarcomeric and cytoskeleton proteins, which then decreases the need for ineffective rounds of subsequent synthesis and turnover. In keeping with this, slowing protein translation with rapamycin can restore translational fidelity in mTOR activated embryonic fibroblasts and can rescue multiple preclinical models of LVF.[46-48] Likewise, in rat PAB, rapamycin was shown to abrogate RV hypertrophy and contractile dysfunction.[46] Although neither protein translation or UPS activity was directly measured in that study, rapamycin further increased PAB-induced ubiquitinated protein accumulation suggesting a decrease in UPS-mediated clearance, which may be the result of improved translation quality. While proteostatic disruption is an established aspect of heart failure and its implication in RVF pathogenesis is growing, it remains unclear how to

therapeutically target this disruption.[49-51] Restoring a conceptual ideal proteostatic balance would require careful titration of the multiple processes involved or elimination of a purely pathologic player. In humans, ROR2 is otherwise broadly absent from healthy mature tissues with its only other well recognized induction occurring in a variety of cancers.[19] Thus, we conclude that ROR2 offers a highly tractable RVF therapeutic target to restore proteostatic balance, which may not require the same level of cardiac-specific delivery in contrast to other molecular targets.

Limitations

More work will be necessary to fully establish the therapeutic potential for targeting ROR2 in RVF pathogenesis. In contrast to our study, in a prior mouse model of myocardial infarction, inducible total body knockout of both ROR1 and ROR2 was associated with lethality from the loss of early myofibroblast activation and hyperinflammation.[22] The differences between that study and ours may be due to multiple factors including total body knockout of both proteins in contrast to knockdown of only ROR2 and by differences in the models studied (RV vs LV pressure overload and the implicated cell populations) conferring altered impact of ROR2 loss. Future work will require understanding the tolerance and therapeutic benefit of complete cardiomyocyte *Ror2* knockout in PAB mice or the therapeutic window for knocking down or inhibiting ROR2 (e.g. using a conditionally active antibody against ROR2 which is being studied in the role of carcinoma).[52]

Conclusions

In summary, we find compelling evidence to implicate ROR2 in RVF pathogenesis. Pathologic reactivation of ROR2 causes proteostatic disruption in the RV, leading to RVF. We propose inhibition or knockdown of ROR2 as a potential therapeutic strategy to restore proteostatic balance and treat RVF, for which no specific therapies currently exist.

Detailed Methods

In vitro experiments

NRVM culture

All animal work was performed under University of Pennsylvania Institutional Animal Care and Use Committee approved protocols (#805255 and #805309). Neonatal rat ventricular myocytes (NRVMs) were isolated and maintained in culture as previously described.[17] Briefly, 1-2 day old Sprague Dawley rat pups were anesthetized on ice, rapidly decapitated and their hearts were excised and placed in chilled Hanks' Balanced Salt Solution (HBSS, Sigma-Aldrich). Ventricular tissues were pooled from a single litter, minced and digested in HBSS with trypsin (Worthington Biochemical) and benzoase (Sigma-Aldrich). Cells were centrifuged at 500g x15 minutes to remove residual trypsin and resuspended in serum-containing NRVM media (DMEM ThermoFisher, 5% FBS, 12.5 mM HEPES (UPenn Cell Center), 4mM Aln-Gln (Sigma-Aldrich), 0.1 mg/mL primocin. Cells were preplated for 2h in cell-culture treated flasks to remove the majority of the cardiac fibroblasts. NRVMs were then plated on plasma treated (PlasmaFlo, Harrick Plasma), collagen-coated nano-patterned culture dishes or coverslips (Curi Bio) at 150,000 cells/cm^2. After overnight attachment in serum-containing media, the cells were serum starved for 48h before further treatment (serum-free media: DMEM, 1X insulin-transferrin-selenium (ThermoFisher), 12.5 mM HEPES, 4mM Aln-Gln, 0.1 mg/mL primocin, 0.3% BSA.

NRVMs were maintained in serum-free NRVM media throughout remaining experiments with media changes every 48 hours. Where indicated, NRVMs were treated with MG132 (1uM or 10uM).

Generating ROR2-modified NRVMs

ROR2 overexpression ($ROR2^{OE}$) NRVMs were generated using adenovirus expressing human *ROR2* under a CMV promoter with an eGFP reporter under a bicistronic CMV promoter (Vector Biolabs ADV-221490) at a multiplicity of infection (MOI) of 100. $ROR2^{KD}$ NRVMs were similarly generated using U6 promoter to express *Ror2* targeting shRNA with a CMV-eGFP (shADV-252440) reporter and control NRVM received virus expressing eGFP alone (cat 1060). For experiments that required the absence of a GFP reporter (see below, GFP-degron), ROR2-OE, $ROR2^{KD}$, and controls NRVMs were generated using adenovirus that did not include a GFP reporter (Vector biolabs: ADV-221490, shADV-252440, and 1640, respectively). $ROR2^{OE}$ and $ROR2^{KD}$ were confirmed by western blot. NRVMs were collected for further analysis 72-hours after adenovirus infection. For experiments with proteasome inhibition, NRVMs were treated with 10μM MG132 in DMSO for short exposures or 1μM DMSO for 24 hours prior to collection. For experiments with concomitant HSP70 overexpression, 48 hours after initial adenovirus treatment NRVMs were then incubated with Ad-mCherry-h-*HSPA1B* (Vector biolabs: ADV-232159) at MOI of 100 for 24 hours prior to cell collection.

shRNA *Ror2*:

5'-CCGG-CGTGGTGCTTTACGCAGAATACTCGAGTATTCTGCGTAAAGCACCACG-TTTTT-3'

shRNA scramble:

5'-GACACGCGACTTGTACCACTTCAAGAGAGTGGTACAAGTCGCGTGTCTTTTTTACGCGT-3'

NRVM RNAseq

NRVMs lysates were collected in RNAlater™ (ThermoFisher) stabilization fluid and total RNA were extracted using RNeasy Mini Kit (Qiagen). RNA samples were diluted to 100 ng/µL by DEPC water using Qubit fluorometer (Thermo Fisher Scientific Waltham, MA). RNAseq was performed by Azenta with PolyA selection on an Illumina HiSeq using 150 bp paired end reads. The paired-ended RNAseq reads were aligned to the rat reference genome (Rnor-6.0) using STAR (version 2.7.9a)(https://pubmed.ncbi.nlm.nih.gov/23104886/). We used Fastqc (version 0.11.7) (https://www.bioinformatics.babraham.ac.uk/projects/fastqc/) to check the quality of the reads, Picard (https://broadinstitute.github.io/picard/) to mark the duplicates, compute the RNAseq metrics and estimate the library complexity. We then calculated the raw read counts using the Rsubread package (version 2.0.3) (https://academic.oup.com/nar/article/47/8/e47/5345150). Genes with 25% of samples having a CPM <1 were considered as low-expressed and were removed from further analysis. We used the voom function from the Limma package (version 3.56.1) to transform and normalize the data, and the toptable function to output the differential analysis result.

Gene set enrichment analysis was performed using Enrichr with genes exhibiting an adjusted $p<0.05$ comparing $ROR2^{OE}$ and $ROR2^{KD}$. To specifically compare these differential expression

data to the cardiac-specific canonical Wnt targets, we downloaded the RNAseq counts file from the GEO Dataset GSE121234 which includes data from a cardiomyocyte-specific non-degradable β-catenin gain of function mouse (Myh6$^{Mer\text{-}Cre\text{-}Mer}$x β-catenin$^{\Delta Ex3}$) and wild type P6 ventricular myocardium. We performed a similar Limma/Voom differential expression analysis and filtered for all commonly identified genes as the background list and adj $p<0.1$ for statistically significant genes.

NRVM Immunofluorescence Microscopy

NRVMs were washed in PBS and fixed in 4% PFA (Electron Microscopy Sciences) for 15 minutes, washed twice with PBS, permeabilized in 0.1% TritonX-100 for 10 minutes at RT, and washed twice with PBS. NRVMs were blocked using Seablock (Abcam) for 1 hour at RT and then incubated in primary antibody diluted in Seablock for 48 hours at 4°C. NRVMs were washed twice with PBS and then incubated in secondary antibody for 24 hours at 4°C. NRVMs were washed twice in PBS, incubated in 1:1000 Hoechst 33342, trihydrochloride, trihydrate (Invitrogen H3570) for 10 minutes at RT, washed twice with PBS, and then mounted onto coverslips using Prolonged Diamond.

NRVMs were imaged on a Zeiss 880 Airyscan confocal microscope operating on an Axiovert Z1 inverted microscope equipped with Plan-Apochromat x63 oil 1.4 numerical aperture objective. Image analysis was performed using ZEN Black software for Airyscan processing to integrate 32 separate sub-resolution detectors in the Airyscan detector and subsequent deconvolution. A z-stack of four 1μM thick slices and 2x2 tiles were captured for each coverslip acquired at regions with representative cell density. Stitching was performed using ZEN Black software.

Further image processing and quantification was performed using FIJI. Each z-stack was converted to a maximum intensity projection. Every NRVM with complete edges visualized in the image were quantified without exclusion. The alpha-actinin or phalloidin channel was used to trace the cell border to generate regions of interest (ROIs). The peripheral ROI for each cell was generated using a FIJI macro to reduce the cell ROI by 2μM in all directions ("AutoShrink", enlarge=-2). NRVM structure was quantified using area, major and minor axes, and aspect ratio. Staining was measured using mean intensity for the entire ROI. To assess peripheral staining enrichment, the difference in raw integrated density between the full ROI and inner ROI was normalized to the difference in area between these ROIs and by the mean intensity for the inner ROI.

NRVM Protein Extraction

NRVMs were washed in PBS and total protein was extracted by scraping and pipetting in extraction buffer: 8M urea, 2M thiourea, 3% sodium dodecylsulfate, 75 mM dithiothreitol, and 50 mM Tris pH 7.5.[54] The extraction buffer was deionized using mixed-bed resin (Biorad, catalog no 1426425) and supplemented with protease/phosphatase inhibitor (Halt™ Protease and Phosphatase Inhibitor Cocktail, ThermoFisher). Cell lysates were mixed 1:1 with 50% glycerol in water.

Proteasome activity quantification

Activity of the ubiquitin proteasome system (UPS) in NRVMs was evaluated using the fluorogenic substrate Suc-LLVY-AMC.[55]

Chymotrypsin-like proteasome activity

Crude lysates from ROR2^{OE,} ROR2^{KD}, and GFP-control NRVMs were collected in NP-40 cell lysis buffer (Invitrogen FNN0021) using sonication at 4°C. Cell lysates were clarified by centrifugation at 10,000G x 10 min at 4°C, and supernatant was collected. Protein quantification was performed by BCA assay and samples were diluted to 0.8 µg/µL. Chymostrypin-like proteasome activity was directly measured using the fluorogenic peptide substrate Suc-LLVY-AMC as follows: 200µL of assay buffer (50mM HEPES pH7.5, 20 mM KCl, 5mM MgCl2, and 1 mM DTT in ddH20) was added to each well of a 96-well black bottom polystyrene plate (Thermo Scientific, cat 137101). Either 10 µL of assay buffer or the chymotrypsin-like specific inhibitor Lactacystin (final concentration 18µM) was added to each well. Either 10µL of assay buffer or ATP to final concentration of 7 µM was added. 10µL of sample was added followed by 10 µL of Suc-LLVY-AMC (final concentration 19.5 µM). Technical replicates were performed in duplicate and averaged. Fluorescence was measured every 1 minute for 45 minutes on a BioTek Synergy Neo2 Plate Reader at 37°C. The difference in fluorescence intensity without and with lactacystin for each timepoint was plotted, and the area on the under the curve was used to determine proteasome activity.

Proteasome activity was measured similarly from mouse and human myocardium with a few modifications. Protein extraction from snap-frozen RV myocardium was performed directly in assay buffer and diluted to 2 µg/µL using BCA assay. Fluorescence was measured every 1

minute for 60 minutes. The area under the curve normalized to control samples for the experiment.

Protein synthesis rate quantification

NRVM translation rate was measured by labeling with the tyrosyl-tRNA analogue puromycin labeling.[17] After generating ROR2^{OE}, GFP-ctrl, and ROR2^{KD} NRVMs with or without concomitant HSP70^{OE}, cells were incubated with low dose (1 μM) puromycin for 1 hour at 37C. As a negative control, some wells were simultaneously incubated with cycloheximide (20 ug/mL). Cells were washed with PBS containing cycloheximide and lysates were collected using thiourea. Puromycylated proteins were quantified by western blot using antipuromycin antibody and normalized to total protein loading by ponceau. Protein translation was also measured similarly using radiolabeled methionine (^{35}S-Met) for 1 hour.[56] ^{35}S-Met labeled proteins were quantified using autoradiography and normalized to ponceau.

Luciferase refolding assay

NRVMs cultured on 35-mm nanopatterned dishes NRVM were extracted using 350μL of Passive Lysis buffer (Promega, Inc.) supplemented with 1X protease inhibitor (Halt Protease Inhibitor), and lysates were maintained at on ice.[57] QuantiLum® Recombinant Luciferase protein was 1 mg (supplied as 10 mg/mL) was dissolved in 1mL of passive lysis buffer and heat shocked at 42°C for 15 minutes to denature the protein. The denatured luciferase protein was spiked into the NRVM lysates at a final concentration of 200 ug/mL and incubated at 37°C for 1 hour. 80μL lysate/luciferase renaturing sample was added to a white bottom 96-well plate, then

20μL of luciferase assay reagent was added and mixed. The plate was immediately read on a BioTek Synergy Neo2 Plate Reader at 37ºC

NRVM Contractility and Relaxation Measurements

NRVM were plated on collagen coated 35mm MatTek glass bottom cell culture dishes for $ROR2^{OE}$, $ROR2^{KD}$, and GFP control as above. NRVMs were paced with the Cytocypher apparatus (IonOptix) using 20 V at 2 Hz. For each replicate, 10-20 cardiomyocytes across multiple regions of each dish were analyzed using CytoMotion Pixel Correlation analysis software without excluding any recording. Every NRVM contractility and relaxation were quantitatively assessed using the time to maximal depression and relaxation velocity as well as time to 10%, 50%, and 90% of peak shortening or return to baseline.

Mass Spectrometry for Proteomics

To assess how ROR2 expression affects the proteome in an unbiased manner, tandem mass tag (TMT)-labeled total was performed from $ROR2^{OE}$ and negative-control NRVM lysates according to previously published protocol.[58] Total lysates were collected using TMT-labeling compatible lysis buffer (8M Urea, 200 mM EPPS pH8.5, Roche cOmplete protease inhibitor, Roche PhosSTOP inhibitor, 1% SDS in ddH_2O). Samples were analyzed using Orbitrap Eclipse mass spectrometer.

Sample Preparation for Mass Spectrometry

Samples for protein analysis were prepared essentially as previously described.[58,59] Following lysis, protein precipitation, reduction/alkylation and digestion, peptides were quantified by BCA assay and 150µg of peptide per sample were labeled with TMTPro reagents (Thermo-Fisher) for 2hrs at room temperature. Labeling reactions were quenched with 0.5% hydroxylamine and acidified with TFA. Acidified peptides were combined and desalted by Sep-Pak (Waters). Peptides from the flow-through were further fractionated for full proteome analysis.

Basic pH reversed-phase separation (BPRP)

TMT labeled peptides were solubilized in 5% ACN/10 mM ammonium bicarbonate, pH 8.0 and 300 µg of TMT labeled peptides was separated by an Agilent 300 Extend C18 column (3.5 µm particles, 4.6 mm ID and 250 mm in length). An Agilent 1260 binary pump coupled with a photodiode array (PDA) detector (Thermo Scientific) was used to separate the peptides. A 45-minute linear gradient from 10% to 40% acetonitrile in 10 mM ammonium bicarbonate pH 8.0 (flow rate of 0.6 mL/min) separated the peptide mixtures into a total of 96 fractions (36 seconds). A total of 96 Fractions were consolidated into 24 samples, acidified with 20 µL of 10% formic acid and vacuum dried to completion. Each sample was desalted via Stage Tips and re-dissolved in 5% formic acid/ 5% acetonitrile for LC-MS3 analysis.

Liquid chromatography separation and tandem mass spectrometry

Proteome data were collected on an Orbitrap Lumos mass spectrometer (ThermoFisher Scientific) coupled to a Proxeon EASY-nLC 1000 LC pump (ThermoFisher Scientific). Fractionated peptides were separated using a 180 min gradient at 500 nL/min on a 35 cm column (i.d. 100 µm, Accucore, 2.6 µm, 150 Å) packed in-house. MS1 data were collected in the Orbitrap

(120,000 resolution; maximum injection time 50 ms; AGC 10×10^5). Charge states between 2 and 5 were required for MS2 analysis, and a 180 s dynamic exclusion window was used. Top 10 MS2 scans were performed in the ion trap with CID fragmentation (isolation window 0.5 Da; Rapid; NCE 35%; maximum injection time 35 ms; AGC 1.2×10^4). An on-line real-time search algorithm (Orbiter) was used to trigger MS3 scans for quantification.[60] MS3 scans were collected in the Orbitrap using a resolution of 50,000, NCE of 55%, maximum injection time of 200 ms, and AGC of 3.0×10^5. The close out was set at two peptides per protein per fraction.[60]

Proteomic Data analysis

Raw files were converted to mzXML, and monoisotopic peaks were re-assigned using Monocle.[61] Searches were performed using the Comet search algorithm against a *Rattus norvegicus* database downloaded from Uniprot in 2021. We used a 50 ppm precursor ion tolerance, 1.0005 fragment ion tolerance, and 0.4 fragment bin offset for MS2 scans collected in the ion trap, and 0.02 fragment ion tolerance; 0.00 fragment bin offset for MS2 scans collected in the Orbitrap. TMTpro on lysine residues and peptide N-termini (+304.2071 Da) and carbamidomethylation of cysteine residues (+57.0215 Da) were set as static modifications, while oxidation of methionine residues (+15.9949 Da) was set as a variable modification.

Each run was filtered separately to 1% False Discovery Rate (FDR) on the peptide-spectrum match (PSM) level. Then proteins were filtered to the target 1% FDR level across the entire combined data set. For reporter ion quantification, a 0.003 Da window around the theoretical m/z of each reporter ion was scanned, and the most intense m/z was used. Reporter ion intensities were adjusted to correct for isotopic impurities of the different TMTpro reagents according to

manufacturer specifications. Peptides were filtered to include only those with a summed signal-to-noise (SN) ≥ 160 across all TMT channels. For each protein site, the filtered peptide TMTpro SN values were summed to generate protein quantification values. The signal-to-noise (S/N) measurements of peptides assigned to each protein were summed (for a given protein). These values were normalized so that the sum of the signal for all proteins in each channel was equivalent thereby accounting for equal protein loading. For the final analysis TMT channels 126, 127N, 127C, 128N, 128C, 129N, 132C, 133N, 133C, 134N, 134C, and 135N were used. Differential protein expression was then quantified using the voom function from the Limma package (version 3.56.1) to transform and normalize the expression data. Differential abundance of E3 ubiquitin ligases was performed by comparing the differential abundance to a published comprehensive list of human E3 ligases.[62]

Mouse studies

Postnatal mouse characterization

E18.5 mice were obtained from a timed pregnant C57BL6 mouse. C57BL6 wild type littermates from separate litters were sacrificed at either P2, P7, or P21. After removing the heart, either atria were trimmed off and the ventricular mass was snap frozen in liquid nitrogen or the entire heart was fixed overnight in 4% PFA followed by serial ethanol dehydration. Thiourea buffer was used to extract total protein. Western blotting was performed as below.

ROR2-overexpression mice

Studies were performed in wild type C57/BL6 mice (Jackson Laboratory, Bar Harbor, ME). To generate cardiac ROR2 overexpression, AAV9 expressing HA-tagged mouse *Ror2* or HA-tagged GFP under a CMV reporter were delivered by retroorbital injection (RO) in 4-week old mice. AAV9 dosing was determined by testing 1 to 4e10 genome copies (GC)/g of *Ror2* or GFP that maximized cardiac delivery while minimizing off target expression in quadriceps, liver, and lung by western blot at 2 to 4 weeks after injection. Minimal extracardiac expression was observed in liver or lung, and RV and LV expression was 4 to 5-fold higher than in quadriceps with the highest dose at 4 weeks (**Supplement Fig. 1a**). Thus, we selected 4e10 GC/g for further studies. Mice were randomly selected from each cage to receive either AAV9-GFP or AAV9-ROR2 (2 each per cage). Mice were phenotyped and sacrificed 8-weeks after injection (age 12 weeks).

Mouse pulmonary artery banding

Pulmonary artery banding was performed in 9-week old C57BL/6 mice in accordance with NIH Guidelines on the Use of Laboratory Animals and with approval by the Administrative Panel on Laboratory Animal Care in the University of Pennsylvania Cardiovascular Institute Rodent Cardiovascular Phenotyping Core. The anesthetic procedure included induction with ketamine (100mg/kg body weight) and xylazine (10mg/kg body weight) cocktail (intraperitoneal injection), tracheal intubation with a 20-guage needle, ventilation with a Harvard rodent ventilator (Harvard Apparatus, Holliston, MA) at a rate of 120-180 breaths per minute and tidal volume of 10 uL/g body weight. The main pulmonary artery trunk was dissected from surrounding tissues and constricted with a 7-0 suture tied against a 25-guage needle to generate a severe RVF. The same procedure including dissection was performed for sham mice apart from pulmonary artery ligature. Echocardiograms were performed 14 days after PAB/sham surgery as above. ROR2

knockdown in PAB mice was generated by retroorbital injection of AAV9 to deliver *Ror2*-targeting shRNA with the above sequence used for in vitro knockdown conserved in mouse/rat or scrambled shRNA at a dose of 4e10 GC/g at age 5 weeks with PAB/sham performed at 9 weeks. Mice were randomized to receive shScr vs shROR2 using GraphPad to randomly assign mice to a group for each round of injections.

Mouse Cardiac Phenotyping

Mouse cardiac physiology phenotyping was performed in the University of Pennsylvania Cardiovascular Institute Rodent Cardiovascular Phenotyping Core who were blinded to groups. For echocardiography, mice were sedated using Avertin by intraperitoneal injection and their temperature was maintained on a biofeedback head-pad. Mice were imaged using a MS400 18-38 MHz probe with a Vevo2100 ultrasound. Echocardiography data was analyzed using Vevo Lab software (Visualsonics). RV end diastolic pressure (RVEDP) was measured by advancing a Millar SPR-1000 Mikro-Trip Mouse Pressure Catheter (Millar, Houston Texas) via the right jugular vein until a ventricular wave form was identified. Data was analyzed using LabChart software (AD Instruments, Colorado Springs, CO).

In vivo puromycin labeling

Mice were singly caged just prior to puromycin injection. Mice were injected intraperitoneal with puromycin (40 nmol/g body weight diluted in PBS) using a staggered schedule to allow sufficient time for sacrifice and heart collection to ensure equal periods of puromycin labeling.[17] After 60 ± 1 minute, mice were euthanized and the hearts were dissected as above, snap frozen, and

processed for protein extraction. Puromycin labeling was normalized between $ROR2^{OE}$/GFP, PAB/Sham, and PAB^{shRor2}/PAB^{shScr} for each staggered set of injections.

Mouse heart collection

After euthanasia, total heart mass was assessed after trimming great vessels, and then normalized to tibia length measured with digital calipers. RV and LV mass was assessed after trimming the atria and separating the RV free wall from the septum and LV. For histology, either a 3mm-punch biopsy was collected from the RV and LV free walls, the base of the heart was isolated, or the intact heart was collected and fixed overnight in 4% PFA followed by serial ethanol dehydration. The remaining heart was separated into RV or LV components and snap frozen in liquid nitrogen. Snap frozen tissue was powdered using a liquid nitrogen cooled cryomill (Retsch).

Mouse protein extraction

Protein extraction was performed from snap frozen tissue using a fractionation protocol to separate cytoplasmic from the nuclear/cytoskeleton fractions.[54] Powdered snap frozen tissue was first exposed to a gentle extraction method using 0.5% Triton-X 100 in Rigor buffer (composition: 10mM Tris, 2mM EGTA, 75mM KCl, pH to 7.1) supplemented with protease and phosphatase inhibitors.[54] The tissue was incubated on ice in 20:1 (μL:mg) triton buffer for 30 minutes with inversion and flicking every 3 minutes until all samples were pale. The samples were centrifuged at 5,000G x10 min at 4°C, the supernatant contained cytoplasmic proteins while the nuclear and cytoskeleton protein was retained in the pellet. The supernatant, hereafter

referred to as the nuclear-cytoskeletal depleted ("NCD") fraction was collected and frozen. The pellet was washed in triton buffer and re-centrifuged. This second supernatant was discarded. The remaining pellet was then exposed to a harsher extraction method using TU-buffer (30:1μL:mg of original sample mass) in a Potter-Elvehjem homogenizer to solubilize all remaining proteins. This latter fraction was enriched for nuclear and cytoskeletal proteins hereafter referred to as the nuclear-cytoskeletal enriched ("NCE") fraction (**Supplement Fig 1b/c**).

Mouse cardiac histology

Mouse histology was performed in the Penn CVI Mouse Histology core using antigen retrieval and antibodies listed in **Supplementary Table 1**. For assessment of ubiquitin staining and peripheral beta catenin, microscopy was performed using a representative section on Keyence microscope at 60X magnification. Quantification of HA-tag positive cardiomyocytes for ubiquitin staining and β-catenin localization in longitudinal orientation was performed using FIJI as above for NRVM analyses. RV cardiomyocyte cross-sectional area was quantified using WGA and the HeartJ macro to quantify the minimum Feret Diameter as a metric that is less susceptible to variability in cardiomyocyte orientation in cross-section for an average of ~500 cardiomyocytes/mouse.[53] Total RV area was quantified by imaging the entire heart in a 4-chamber view and then analyzed in FIJI. The epicardial and endocardial borders were defined using colour deconvolution to create a binary mask of the RV and then quantifying this area. For Trichrome and Sirius red percent quantification, a similar method was used to quantify only the area staining positively for fibrosis and normalizing to the total area. RNAscope was performed according to manufacturer instructions using the RNAscope® Multiplex Fluorescent V2 kit (ACD, Newark, CA) and probes to *Ror2*, *Ryr2* to identify cardiomyocytes, and *Dcn* to identify

fibroblasts. DAPI was used to identify nuclei. RNAscope images were captured using Zeiss Airyscan 880 Confocal Microscope.

qPCR

RNA extraction was performed using RNeasy mini kits (Qiagen Hilden, Germany) according to manufacturer instructions. cDNA was made using Applied Biosystems™ High-Capacity cDNA Reverse Transcription Kit (FisherScientific). Gene expression was quantified suing SYBR Green Master Mix RT-PCR. Primer sequences (**Supplementary Table 2**).

Western Blot

Equal amounts of total protein or protein fractions were separated using SDS-page in a 4-20% gradient gel and then transferred to PVDF membrane. Total protein as a loading control was measured using ponceau S stain imaged using ImageQuant™ LAS 4000. Blots were blocked in 3% BSA diluted in PBS for 1 hour at room temperature (RT), incubated overnight in primary antibody, washed in TBS-T for 10 minutes x3, incubated in secondary antibody for 1 hour at RT, and washed in TBS-T for 10 minutes x3. Densitometry was assessed using SuperSignal™ West Femto enhanced chemiluminescent substrate (ThermoFisher Scientific), imaged, and quantified as previously described.[13] Primary and secondary antibodies are listed in **Supplementary Table 1**. Quantification was performed using ImageStudio (LI-COR Biotechnology, Lincoln, Nebraska) or ImageJ.

Human Studies

Procurement of all human RV myocardial tissue was performed in accordance with protocols approved by the University of Pennsylvania Institutional Review Board (approval 802781) and the Gift-of-Life Donor Program, Philadelphia, PA. Prospective informed consent for research use of surgically explanted tissue was obtained from the transplant recipients or from the next-of-kin in the case of deceased organ donors, as previously described.[18] RV myocardial samples were obtained from the Penn Human Heart Tissue Library collected from May 2007 to March 2016.[13] RV myocardium was analyzed from patients with DCM RVF with (n=9) stratified by degree of ROR2 expression, DCM RVs with preserved RV function (n=3), and non-failing (n=6). Patient demographics and clinical data are presented in supplementary data (Supplementary Table 3 and Supplementary Data 1). Representative human samples were selected based upon previously published levels of ROR2 expression.[13] Proteasome activity was measured as described above. Protein fractionation was performed for the RV tissue using Triton/TU separation as above for subsequent western blotting. Histology for RNAscope was performed similarly as for mouse histology using human specific RNAscope probes.

Acknowledgements

We thank Julian Mintseris, Rachel Rodrigues, and Jonathan Van Vraken at Thermo Fisher Scientific Center for Multiplexed Proteomics at Harvard Medical School for support in performing proteomics. We thank the Day Lab at University of Pennsylvania for kindly providing adenovirus to express GFPμ. The mouse PAB and echocardiography were performed by the Rodent Cardiovascular Phenotyping Core (RRID: SCR_022419) at the University of Pennsylvania

supported by the Penn Cardiovascular Institute and NIH S10OD016393. Figures were generated with assistance of BioRender.

Sources of Funding

J.J.E. was supported by NIH K08HL159311. J.J.E and Z.A. was supported by the Children's Hospital of Philadelphia Frontier Program "Advanced Cardiac Therapies for Heart Failure". K.U. was supported by the NIH (T32 HL007843). B.P. was supported by the National Institute of Health (NIH) R01 HL149891 and the Foundation Leducq Research Grant no. 20CVD01. C.S.C. was supported by Department of the Army (HT94252310080) and the NIH R35 GM154896. Human heart tissues were procured with funding support from multiple NIH grants to K.M.: R01 AG017022, R01 HL089847, and R01 HL105993, and R01 HL133080.

Author Contributions

H.H., J.J.E., and Z.A. developed the concept and designed the experiments. J.J.E, Z.A., and B.L.P. supervised and funded the project. J.J.E., H.H., K.U., E.A.S., G.U., S.K., and S.W. conducted NRVM experiments. J.J.E., H.H., and D.E. conducted NRVM contractility/relaxation experiments. J.J.E and H.H. performed mouse experiments. J.J.E, T.D., and C.S.C. conducted luciferase refolding and ^{35}S-Met labeling assays. J.B. and Y.Y. performed RNAseq analysis. L. Lai, J.G., and S.S. performed mouse surgeries and physiologic characterization. K.C.B. and K.M. supported human heart tissue procurement and clinical characterization. H.R. contributed to microscopy image analysis. L.Li performed tissue histology. All authors contributed to the manuscript preparation and approved the final version of the manuscript.

Disclosures

There are no relevant disclosures.

Corresponding author

Correspondence to Jonathan J. Edwards and Zoltan P. Arany.

References

1 Lampert, B. C. & Teuteberg, J. J. Right ventricular failure after left ventricular assist devices. *J Heart Lung Transplant* **34**, 1123-1130 (2015). https://doi.org/10.1016/j.healun.2015.06.015

2 Zakeri, R. & Mohammed, S. F. Epidemiology of Right Ventricular Dysfunction in Heart Failure with Preserved Ejection Fraction. *Curr Heart Fail Rep* **12**, 295-301 (2015). https://doi.org/10.1007/s11897-015-0267-3

3 Khairy, P. *et al.* Long-term survival, modes of death, and predictors of mortality in patients with Fontan surgery. *Circulation* **117**, 85-92 (2008). https://doi.org/10.1161/CIRCULATIONAHA.107.738559

4 Piran, S., Veldtman, G., Siu, S., Webb, G. D. & Liu, P. P. Heart failure and ventricular dysfunction in patients with single or systemic right ventricles. *Circulation* **105**, 1189-1194 (2002).

5 Campo, A. *et al.* Outcomes of hospitalisation for right heart failure in pulmonary arterial hypertension. *Eur Respir J* **38**, 359-367 (2011). https://doi.org/10.1183/09031936.00148310

6 Babu-Narayan, S. V. *et al.* Randomised trial of ramipril in repaired tetralogy of Fallot and pulmonary regurgitation: the APPROPRIATE study (Ace inhibitors for Potential PRevention Of the deleterious effects of Pulmonary Regurgitation In Adults with repaired TEtralogy of Fallot). *Int J Cardiol* **154**, 299-305 (2012). https://doi.org/10.1016/j.ijcard.2010.09.057

7 Dos, L. *et al.* Eplerenone in systemic right ventricle: double blind randomized clinical trial. The evedes study. *Int J Cardiol* **168**, 5167-5173 (2013). https://doi.org/10.1016/j.ijcard.2013.07.163

8 Doughan, A. R., McConnell, M. E. & Book, W. M. Effect of beta blockers (carvedilol or metoprolol XL) in patients with transposition of great arteries and dysfunction of the

systemic right ventricle. *Am J Cardiol* **99**, 704-706 (2007). https://doi.org/10.1016/j.amjcard.2006.10.025

9 Shaddy, R. E. *et al.* Carvedilol for children and adolescents with heart failure: a randomized controlled trial. *JAMA* **298**, 1171-1179 (2007). https://doi.org/10.1001/jama.298.10.1171

10 Bokma, J. P. *et al.* Effect of Losartan on Right Ventricular Dysfunction: Results From the Double-Blind, Randomized REDEFINE Trial (Right Ventricular Dysfunction in Tetralogy of Fallot: Inhibition of the Renin-Angiotensin-Aldosterone System) in Adults With Repaired Tetralogy of Fallot. *Circulation* **137**, 1463-1471 (2018). https://doi.org/10.1161/CIRCULATIONAHA.117.031438

11 Roche, S. L. & Redington, A. N. Right ventricle: wrong targets? Another blow for pharmacotherapy in congenital heart diseases. *Circulation* **127**, 314-316 (2013). https://doi.org/10.1161/CIRCULATIONAHA.112.155887

12 Hartupee, J. & Mann, D. L. Neurohormonal activation in heart failure with reduced ejection fraction. *Nat Rev Cardiol* **14**, 30-38 (2017). https://doi.org/10.1038/nrcardio.2016.163

13 Edwards, J. J. *et al.* Noncanonical WNT Activation in Human Right Ventricular Heart Failure. *Front Cardiovasc Med* **7**, 582407 (2020). https://doi.org/10.3389/fcvm.2020.582407

14 Takeuchi, S. *et al.* Mouse Ror2 receptor tyrosine kinase is required for the heart development and limb formation. *Genes Cells* **5**, 71-78 (2000). https://doi.org/10.1046/j.1365-2443.2000.00300.x

15 Guo, R. & Xing, Q. S. Roles of Wnt Signaling Pathway and ROR2 Receptor in Embryonic Development: An Update Review Article. *Epigenet Insights* **15**, 25168657211064232 (2022). https://doi.org/10.1177/25168657211064232

16 Nomi, M. *et al.* Loss of mRor1 enhances the heart and skeletal abnormalities in mRor2-deficient mice: redundant and pleiotropic functions of mRor1 and mRor2 receptor tyrosine kinases. *Mol Cell Biol* **21**, 8329-8335 (2001). https://doi.org/10.1128/MCB.21.24.8329-8335.2001

17 Scarborough, E. A. *et al.* Microtubules orchestrate local translation to enable cardiac growth. *Nat Commun* **12**, 1547 (2021). https://doi.org/10.1038/s41467-021-21685-4

18 Chen, C. Y. *et al.* Suppression of detyrosinated microtubules improves cardiomyocyte function in human heart failure. *Nat Med* **24**, 1225-1233 (2018). https://doi.org/10.1038/s41591-018-0046-2

19 Morioka, K. *et al.* Orphan receptor tyrosine kinase ROR2 as a potential therapeutic target for osteosarcoma. *Cancer Sci* **100**, 1227-1233 (2009). https://doi.org/10.1111/j.1349-7006.2009.01165.x

20 Chaffin, M. *et al.* Single-nucleus profiling of human dilated and hypertrophic cardiomyopathy. *Nature* **608**, 174-180 (2022). https://doi.org/10.1038/s41586-022-04817-8

21 Litvinukova, M. *et al.* Cells of the adult human heart. *Nature* **588**, 466-472 (2020). https://doi.org/10.1038/s41586-020-2797-4

22 Chavkin, N. W. *et al.* The Cell Surface Receptors Ror1/2 Control Cardiac Myofibroblast Differentiation. *J Am Heart Assoc* **10**, e019904 (2021). https://doi.org/10.1161/JAHA.120.019904

23 Sahu, I. *et al.* The 20S as a stand-alone proteasome in cells can degrade the ubiquitin tag. *Nat Commun* **12**, 6173 (2021). https://doi.org/10.1038/s41467-021-26427-0

24 Jurida, L. *et al.* A common gene signature of the right ventricle in failing rat and human hearts. *Nature Cardiovascular Research* **3**, 819-840 (2024). https://doi.org/10.1038/s44161-024-00485-1

25 Holzem, M., Boutros, M. & Holstein, T. W. The origin and evolution of Wnt signalling. *Nat Rev Genet* **25**, 500-512 (2024). https://doi.org/10.1038/s41576-024-00699-w

26 Debebe, Z. & Rathmell, W. K. Ror2 as a therapeutic target in cancer. *Pharmacol Ther* **150**, 143-148 (2015). https://doi.org/10.1016/j.pharmthera.2015.01.010

27 Castro, M. V. & Lopez-Bergami, P. Cellular and molecular mechanisms implicated in the dual role of ROR2 in cancer. *Crit Rev Oncol Hematol* **170**, 103595 (2022). https://doi.org/10.1016/j.critrevonc.2022.103595

28 Ford, C. E., Qian Ma, S. S., Quadir, A. & Ward, R. L. The dual role of the novel Wnt receptor tyrosine kinase, ROR2, in human carcinogenesis. *Int J Cancer* **133**, 779-787 (2013). https://doi.org/10.1002/ijc.27984

29 Li, R. *et al.* ROR2 induces cell apoptosis via activating IRE1alpha/JNK/CHOP pathway in high-grade serous ovarian carcinoma in vitro and in vivo. *J Transl Med* **17**, 428 (2019). https://doi.org/10.1186/s12967-019-02178-x

30 Hagenmueller, M. *et al.* Dapper-1 is essential for Wnt5a induced cardiomyocyte hypertrophy by regulating the Wnt/PCP pathway. *FEBS Lett* **588**, 2230-2237 (2014). https://doi.org/10.1016/j.febslet.2014.05.039

31 Zhang, P. *et al.* Vangl2 is essential for myocardial remodeling activated by Wnt/JNK signaling. *Exp Cell Res* **365**, 33-45 (2018). https://doi.org/10.1016/j.yexcr.2018.02.012

32 Landin Malt, A. *et al.* Non-Canonical Wnt Signaling Regulates Cochlear Outgrowth and Planar Cell Polarity via Gsk3beta Inhibition. *Front Cell Dev Biol* **9**, 649830 (2021). https://doi.org/10.3389/fcell.2021.649830

33 Wu, D. & Pan, W. GSK3: a multifaceted kinase in Wnt signaling. *Trends Biochem Sci* **35**, 161-168 (2010). https://doi.org/10.1016/j.tibs.2009.10.002

34 Zhai, P., Sciarretta, S., Galeotti, J., Volpe, M. & Sadoshima, J. Differential roles of GSK-3beta during myocardial ischemia and ischemia/reperfusion. *Circ Res* **109**, 502-511 (2011). https://doi.org/10.1161/CIRCRESAHA.111.249532

35 Stretton, C. *et al.* GSK3-mediated raptor phosphorylation supports amino-acid-dependent mTORC1-directed signalling. *Biochem J* **470**, 207-221 (2015). https://doi.org/10.1042/BJ20150404

36 Robertson, H., Hayes, J. D. & Sutherland, C. A partnership with the proteasome; the destructive nature of GSK3. *Biochem Pharmacol* **147**, 77-92 (2018). https://doi.org/10.1016/j.bcp.2017.10.016

37 Kwak, D. *et al.* Osmotic stress regulates mammalian target of rapamycin (mTOR) complex 1 via c-Jun N-terminal Kinase (JNK)-mediated Raptor protein phosphorylation. *J Biol Chem* **287**, 18398-18407 (2012). https://doi.org/10.1074/jbc.M111.326538

38 Kim, Y. K. *et al.* Deletion of the inducible 70-kDa heat shock protein genes in mice impairs cardiac contractile function and calcium handling associated with hypertrophy. *Circulation* **113**, 2589-2597 (2006). https://doi.org/10.1161/CIRCULATIONAHA.105.598409

39 van der Pol, A., Hoes, M. F., de Boer, R. A. & van der Meer, P. Cardiac foetal reprogramming: a tool to exploit novel treatment targets for the failing heart. *J Intern Med* **288**, 491-506 (2020). https://doi.org/10.1111/joim.13094

40 Poon, E. *et al.* Proteomic Analysis of Human Pluripotent Stem Cell-Derived, Fetal, and Adult Ventricular Cardiomyocytes Reveals Pathways Crucial for Cardiac Metabolism and Maturation. *Circ Cardiovasc Genet* **8**, 427-436 (2015). https://doi.org/10.1161/CIRCGENETICS.114.000918

41 Nagai, R., Low, R. B., Stirewalt, W. S., Alpert, N. R. & Litten, R. Z. Efficiency and capacity of protein synthesis are increased in pressure overload cardiac hypertrophy. *Am J Physiol* **255**, H325-328 (1988). https://doi.org/10.1152/ajpheart.1988.255.2.H325

42 Lewis, Y. E. *et al.* Localization of transcripts, translation, and degradation for spatiotemporal sarcomere maintenance. *J Mol Cell Cardiol* **116**, 16-28 (2018). https://doi.org/10.1016/j.yjmcc.2018.01.012

43 Pervolaraki, E., Dachtler, J., Anderson, R. A. & Holden, A. V. The developmental transcriptome of the human heart. *Sci Rep* **8**, 15362 (2018). https://doi.org/10.1038/s41598-018-33837-6

44 Kotter, S. & Kruger, M. Protein Quality Control at the Sarcomere: Titin Protection and Turnover and Implications for Disease Development. *Front Physiol* **13**, 914296 (2022). https://doi.org/10.3389/fphys.2022.914296

45 Chorghade, S. *et al.* Poly(A) tail length regulates PABPC1 expression to tune translation in the heart. *Elife* **6** (2017). https://doi.org/10.7554/eLife.24139

46 Harston, R. K. *et al.* Rapamycin treatment augments both protein ubiquitination and Akt activation in pressure-overloaded rat myocardium. *Am J Physiol Heart Circ Physiol* **300**, H1696-1706 (2011). https://doi.org/10.1152/ajpheart.00545.2010

47 Fleming, N. D., Samsa, L. A., Hassel, D., Qian, L. & Liu, J. Rapamycin attenuates pathological hypertrophy caused by an absence of trabecular formation. *Sci Rep* **8**, 8584 (2018). https://doi.org/10.1038/s41598-018-26843-1

48 Li, S. *et al.* Mechanism of Eccentric Cardiomyocyte Hypertrophy Secondary to Severe Mitral Regurgitation. *Circulation* **141**, 1787-1799 (2020). https://doi.org/10.1161/CIRCULATIONAHA.119.043939

49 Buhringer, H., Doroudgar, S., Wang, X., Frey, N. & Rangrez, A. Y. Editorial: Proteostasis in cardiac health and disease. *Front Mol Biosci* **11**, 1433721 (2024). https://doi.org/10.3389/fmolb.2024.1433721

50 Heitmeier, T. *et al.* Altered proteasome function in right ventricular hypertrophy. *Cardiovasc Res* **116**, 406-415 (2020). https://doi.org/10.1093/cvr/cvz103

51 Rajagopalan, V. *et al.* Altered ubiquitin-proteasome signaling in right ventricular hypertrophy and failure. *Am J Physiol Heart Circ Physiol* **305**, H551-562 (2013). https://doi.org/10.1152/ajpheart.00771.2012

52 *A Phase 2 Open Label Study of BA3021 in Patients With Recurrent or Metastatic Squamous Cell Carcinoma of the Head and Neck*, <https://www.clinicaltrials.gov/study/NCT05271604> (

53 Droste, P. *et al.* Semiautomated pipeline for quantitative analysis of heart histopathology. *J Transl Med* **21**, 666 (2023). https://doi.org/10.1186/s12967-023-04544-2

54 McAfee, Q. *et al.* Truncated titin proteins in dilated cardiomyopathy. *Sci Transl Med* **13**, eabd7287 (2021). https://doi.org/10.1126/scitranslmed.abd7287

55 Dong, X. *et al.* In situ dynamically monitoring the proteolytic function of the ubiquitin-proteasome system in cultured cardiac myocytes. *Am J Physiol Heart Circ Physiol* **287**, H1417-1425 (2004). https://doi.org/10.1152/ajpheart.01233.2003

56 Rabkin, S. W., Lodha, P. & Kong, J. Y. Reduction of protein synthesis and statin-induced cardiomyocyte cell death. *Cardiovasc Toxicol* **7**, 1-9 (2007). https://doi.org/10.1007/s12012-007-0003-7

57 Conn, C. S. & Qian, S. B. Nutrient signaling in protein homeostasis: an increase in quantity at the expense of quality. *Sci Signal* **6**, ra24 (2013). https://doi.org/10.1126/scisignal.2003520

58 Navarrete-Perea, J., Yu, Q., Gygi, S. P. & Paulo, J. A. Streamlined Tandem Mass Tag (SL-TMT) Protocol: An Efficient Strategy for Quantitative (Phospho)proteome Profiling Using Tandem Mass Tag-Synchronous Precursor Selection-MS3. *J Proteome Res* **17**, 2226-2236 (2018). https://doi.org/10.1021/acs.jproteome.8b00217

59 Li, J. *et al.* TMTpro-18plex: The Expanded and Complete Set of TMTpro Reagents for Sample Multiplexing. *J Proteome Res* **20**, 2964-2972 (2021). https://doi.org/10.1021/acs.jproteome.1c00168

60 Schweppe, D. K. *et al.* Full-Featured, Real-Time Database Searching Platform Enables Fast and Accurate Multiplexed Quantitative Proteomics. *J Proteome Res* **19**, 2026-2034 (2020). https://doi.org/10.1021/acs.jproteome.9b00860

61 Rad, R. *et al.* Improved Monoisotopic Mass Estimation for Deeper Proteome Coverage. *J Proteome Res* **20**, 591-598 (2021). https://doi.org/10.1021/acs.jproteome.0c00563

62 Medvar, B., Raghuram, V., Pisitkun, T., Sarkar, A. & Knepper, M. A. Comprehensive database of human E3 ubiquitin ligases: application to aquaporin-2 regulation. *Physiol Genomics* **48**, 502-512 (2016). https://doi.org/10.1152/physiolgenomics.00031.2016

Figures Legends

Fig. 1 ROR2 is a developmentally restricted protein that is robustly upregulated in RVF. (**a**) ROR2 protein expression measured by western blot naturally tapers from P2 to P21 and is retained modestly in the atria (N=3-7/age group; statistics by One-Way ANOVA with Dunnet's comparison against P1). (**b**) By histology ROR2 was observed to localize to cardiomyocytes cell membrane and nucleus. (**c-f**) PAB causes RV remodeling and dysfunction, (G, 10X magnification) fibrosis and (**h/i**) induction of classic heart failure markers fetal MYH7 and *Nppb*. The normally developmentally restricted Ror2 is robustly increased in the NCD (cytoplasmic) and the NCE fractions (triton-insoluble) (**j-l**). By immunohistochemistry (**m**, 20X magnification) and RNAscope (**n**, 63X magnification), Ror2 localizes to both cardiomyocytes and fibroblasts in PAB RV. Statistics for PAB analyses by unpaired t-test or Mann-Whitney, depending on normality.

Fig. 2 ROR2 regulates in vitro cardiomyocyte morphology and contraction. (**a/b**) NRVMs were cultured on nanopatterned surface and either received adenovirus to overexpress human ROR2, knockdown ROR2, or express GFP alone. (**c-e**, 63X magnification) Modifying ROR2 levels in NRVMs has dramatic effects on morphology including cell size and aspect ratio. (**f-l**) Assessing the peripheral and mean staining for α-actinin, β-catenin, and Cx43 and total expression by western blot reveals that $ROR2^{OE}$ cause preferential loss of the peripheral localization of these proteins while increasing or not changing their total expression. $ROR2^{KD}$ generally causes opposing effects (N=8-9 NRVM isolations, n=341-411/condition for cardiomyocyte morphology and n=3 for western blot with statistics by One-Way ANOVA with Dunnet's multiple comparisons). Using a Cytocypher pacing apparatus, $ROR2^{OE}$ worsened and $ROR2^{KD}$ improved relaxation kinetics (n=26-27/group from two separate NRVM isolations).

Fig. 3 ROR2 regulates in vitro cardiomyocyte proteostasis.

(**a/b**) RNAseq of ROR2^{OE} and ROR2^{KD} NRVMs revealed transcriptional changes in the proteostatic pathways including folding (e.g. *Hspa1a/b, Hsph1, Cryab*) and UPS-mediated protein turnover by pathway enrichment analysis (n=4/group). (**c-e**) Western blot confirmed ROR2^{OE} caused reduction in total ubiquitin and HSP70, both of which were increased in ROR2^{KD}. (**f/g**) Using the proteasome inhibitor MG132, we found that proteasome directing K48-linked ubiquitin was preferentially increased in ROR2^{OE} suggesting increased flux through the UPS. (**h**) Proteasome capacity was measured using the UPS- substrate peptide Suc-LLVY-AMC with cell lysates, ROR2^{KD} reduces maximal proteasome capacity in absence and presence of ATP supplementation (n=3-4). (**i/j**) Protein synthesis by puromycin and ^{3}5S-Met labeling was increased in ROR2^{OE} and reduced in ROR2^{KD}. (**k/l)** HSP70^{OE} did not prevent ROR2^{OE}-responsive increase in protein synthesis, but did increase ubiquitin accumulation, suggesting a possible improvement in protein quality and reduced UPS-turnover. (**m**) Protein refolding of heat shocked luciferase measured by its ability to cleave luciferin was impaired in ROR2^{OE} lysates compared to ROR2^{KD} (n=7/group). Statistical comparisons were performed with One ANOVAs, except for proteasome capacity analysis for which a Two-Way ANOVA comparing group and ATP interaction, with Tukey's multiple comparisons.

Fig. 4 ROR2 mediated proteostatic disruption impacts cardiomyocyte structural proteins

The interaction of ROR2^{OE} and proteasome inhibition on the impact of the NRVM proteome was investigated by proteomics. (**a-c**) By volcano plot and PCA plot we reveal that ROR2^{OE} dramatically changes the global proteome, which is partially mitigated by proteasome inhibition by MG132. (**d/e**) ROR2^{OE} dramatically changes the E3 ubiquitin ligase expression profile as illustrated by dotplot and heatmap. (**f/g**) Pathway enrichment of DEPs reveal broad changes in proteome including downregulation of actin/sarcomeric proteins, which is largely reversed by proteasome inhibition.

Fig. 5 Cardiac ROR2 induction is sufficient to cause RVF and proteostatic disruption in mice. (**a**) The impact of cardiac ROR2^{OE} was tested using AAV9 delivery of *Ror2* vs GFP in male and female mice. Cardiac ROR2^{OE} caused a male predominant phenotype with increase in heart size (**b**, 10X magnification) driven by an increase in RV wall area (**c**) with an increase in total heart and RV mass (**d/e**) but not LV mass (**f**). This was associated with an increase in RV cross sectional area by minimum Feret Diameter using HeartJ[53] (**g/h**, 40X magnification). Male mice also showed biventricular dilation and systolic dysfunction by echocardiography (**i-l**) and an increase in RV end diastolic pressure by jugular catheterization (**m**). Ror2^{OE} also caused a modest induction in *Nppb* (**n**) and fetal MYH7 (**o**) without increasing fibrosis (**p**). Proteostatic characterization revealed a decrease in *Hspa1b* (**q**), decrease in ubiquitin staining (**r/s**, 60X magnification), increase in protein translation (**t**) and increase in proteasome capacity (**u**). Statistical comparisons performed using t-test or Mann Whitney depending on normality, (n=3-8 mice/group and 32-72 RV cardiomyocytes/group for panel **s**).

Fig. 6 ROR2 knockdown improves RVF and proteostatic burden in RV pressure overload. (**a-g**) PAB compared to sham mice revealed broad dysregulation in proteostatic state with increase in protein synthesis by puromycin labeling, HSP70 expression, proteasome expression and capacity, and total ubiquitin without altering K48 ubiquitin levels. (**h**) $ROR2^{KD}$ was achieved by AAV9-delivery of *Ror2* targeting shRNA (PAB^{shRor2}) which reduced NCD (~25%) and NCE (~50%) ROR2 expression compared to scrambled shRNA (PAB^{Scr}; **i/j**). (**k-m**) By echocardiogram PAB^{shRor2}, showed reduced RV dilation, systolic and diastolic dysfunction. (**n-p**) PAB^{shRor2} exhibited less fibrosis and RV hypertrophy (10X magnification). (**q-t**) PAB^{shRor2} demonstrated reduced proteostatic burden with less protein synthesis and HSP70 induction without affecting proteasome capacity, resulting in reduced K48 ubiquitin accumulation. Statistics by t-test or Mann Whitney depending on normality (n=3-9 for Sham vs PAB and n=6-15 for PAB^{shRor2} vs PAB^{shScr}).

Fig. 7 Model of ROR2-driven proteostatic disruption in RVF. ROR2 expression is associated with proteostatic disruption in human RVF. (**a**) RVF in humans from dilated cardiomyopathy with high (red) or low (blue) ROR2 expression were compared to dilated cardiomyopathy with preserved RV function (pRV, orange) and nonfailing (NF, black) RVs from discarded donors as have been previously characterized.[13] ROR2 expression was quantified in NCD (cytoplasmic) and NCE fractions. (**b/c**) Higher ROR2 expression was associated with evidence of proteostatic dysfunction with an increase in proteasome capacity that correlated to levels of ROR2 in the NCE fraction. Statistics by One Way ANOVA with Tukey's multiple comparisons or Kruskal-Wallis with Dunn's multiple comparisons (n=3-6/group) and Pearson correlation coefficient (in panel C, the patient with high NCD but low NCE ROR2 is denoted by a purple star). (**d**) Taken together, our work reveals a model wherein high ROR2 expression in cardiomyocytes disrupts proteostasis with increased protein synthesis (1) and reduced folding (2) that results in a poor-quality proteome, leading cardiomyocytes to clear proteins by the UPS (3), which disrupts cardiomyocyte structure and function (4).

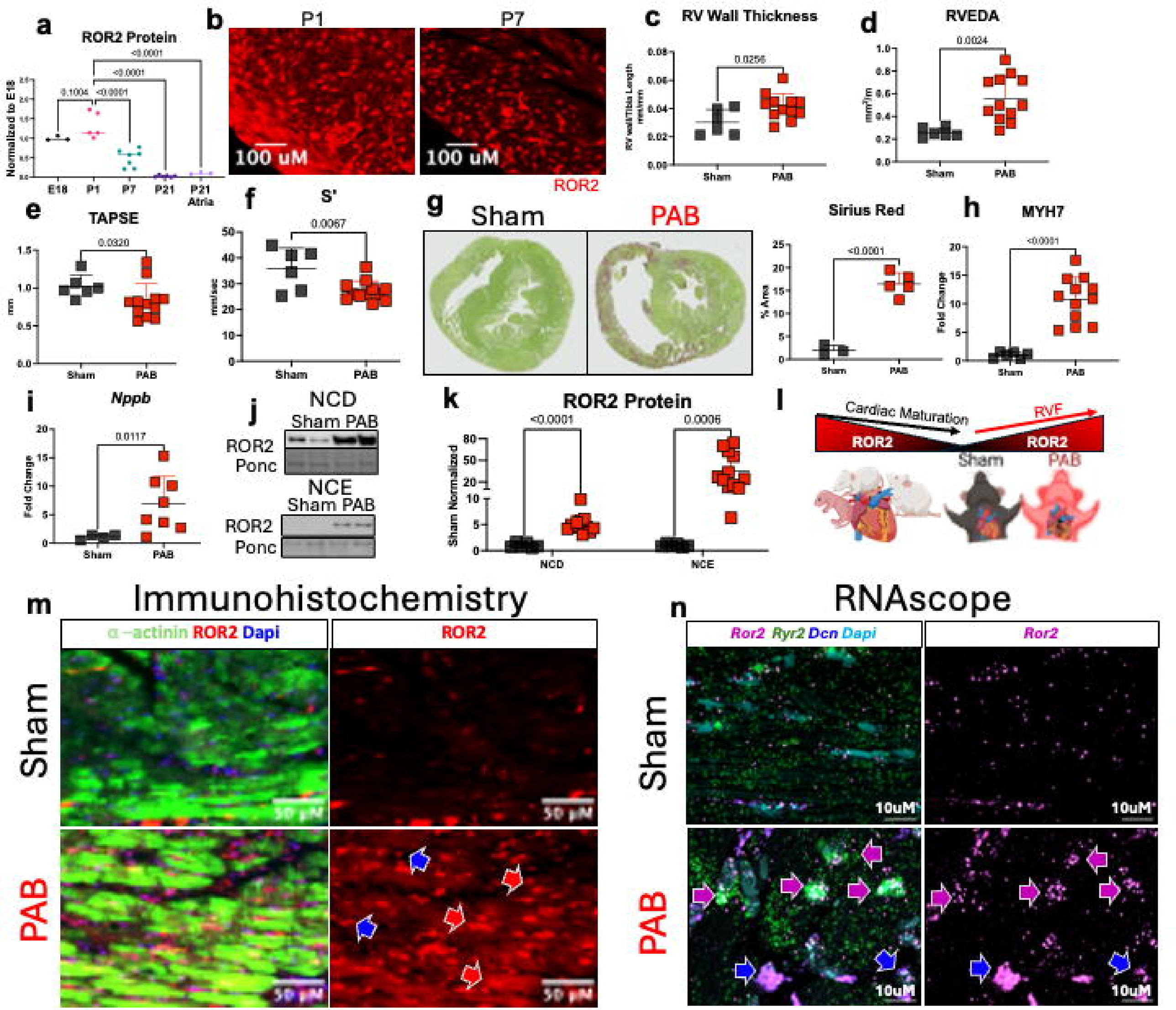
a
ROR2 Protein
Normalized to E18
<0.0001
<0.0001
0.1004
<0.0001
E18
P1
P7
P21
P21 Atria
b
P1
P7
100 uM
100 uM
ROR2
c
RV Wall Thickness
RV wall/Tibia Length mm/mm
0.0256
Sham
PAB
d
RVEDA
mm²/m
0.0024
Sham
PAB
e
TAPSE
mm
0.0320
Sham
PAB
f
S'
mm/sec
0.0067
Sham
PAB
g
Sham
PAB
Sirius Red
% Area
<0.0001
Sham
PAB
h
MYH7
Fold Change
<0.0001
Sham
PAB
i
Nppb
Fold Change
0.0117
Sham
PAB
j
NCD
Sham PAB
ROR2
Ponc
NCE
Sham PAB
ROR2
Ponc
k
ROR2 Protein
Sham Normalized
<0.0001
0.0006
NCD
NCE
l
Cardiac Maturation
RVF
ROR2
ROR2
Sham
PAB
m
Immunohistochemistry
α -actinin ROR2 Dapi
ROR2
Sham
PAB
50 μM
n
RNAscope
Ror2 Ryr2 Dcn Dapi
Ror2
Sham
PAB
10uM

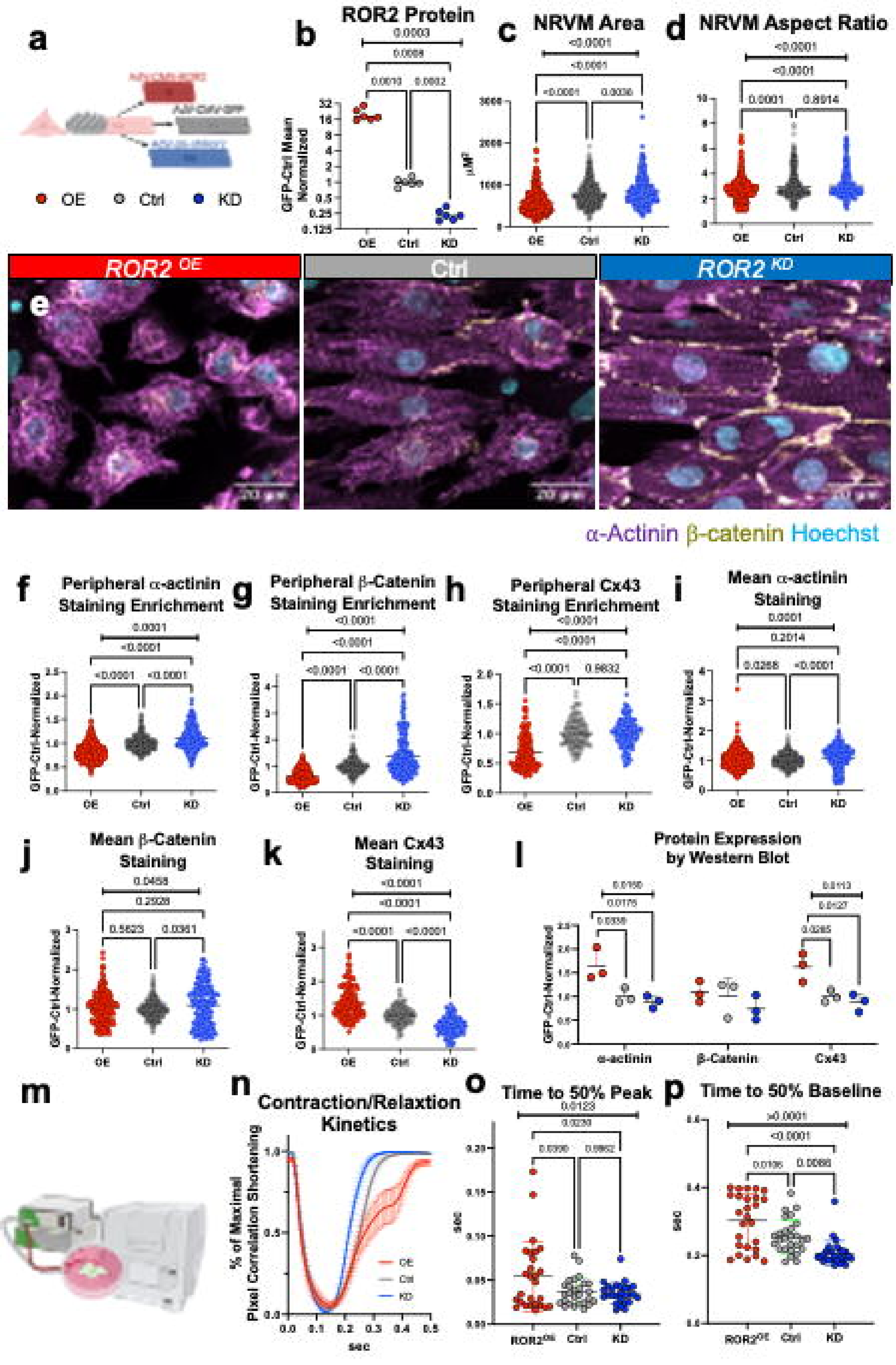
a
OE
Ctrl
KD
b
ROR2 Protein
GFP-Ctrl Mean Normalized
c
NRVM Area
d
NRVM Aspect Ratio
e
ROR2 OE
Ctrl
ROR2 KD
α-Actinin β-catenin Hoechst
f
Peripheral α-actinin Staining Enrichment
g
Peripheral β-Catenin Staining Enrichment
h
Peripheral Cx43 Staining Enrichment
i
Mean α-actinin Staining
j
Mean β-Catenin Staining
k
Mean Cx43 Staining
l
Protein Expression by Western Blot
α-actinin
β-Catenin
Cx43
m
n
Contraction/Relaxtion Kinetics
% of Maximal Pixel Correlation Shortening
sec
o
Time to 50% Peak
p
Time to 50% Baseline

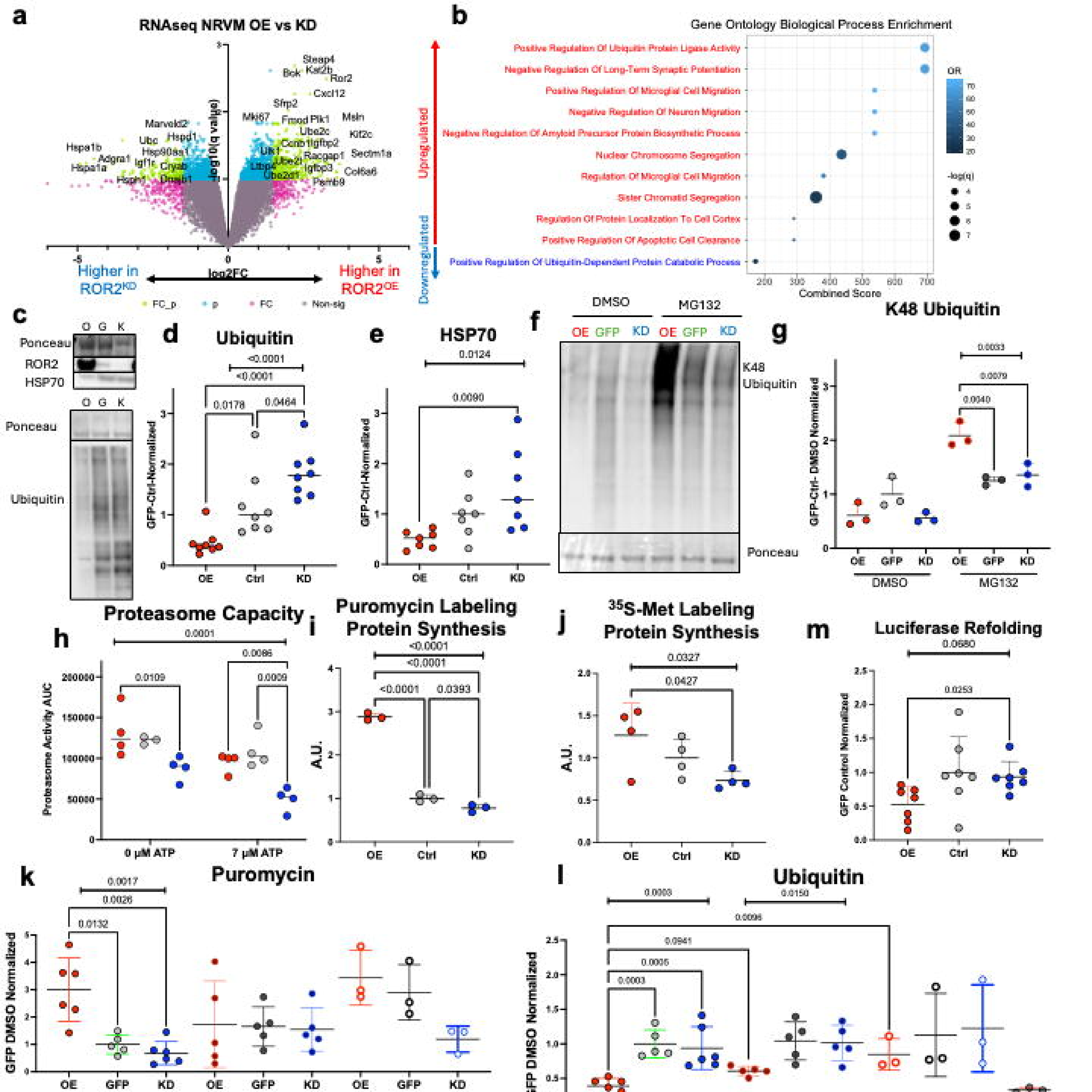

a
RNAseq NRVM OE vs KD
-log10(q value)
log2FC
Higher in ROR2KD
Higher in ROR2OE
FC_p
p
FC
Non-sig
Upregulated
Downregulated
b
Gene Ontology Biological Process Enrichment
Positive Regulation Of Ubiquitin Protein Ligase Activity
Negative Regulation Of Long-Term Synaptic Potentiation
Positive Regulation Of Microglial Cell Migration
Negative Regulation Of Neuron Migration
Negative Regulation Of Amyloid Precursor Protein Biosynthetic Process
Nuclear Chromosome Segregation
Regulation Of Microglial Cell Migration
Sister Chromatid Segregation
Regulation Of Protein Localization To Cell Cortex
Positive Regulation Of Apoptotic Cell Clearance
Positive Regulation Of Ubiquitin-Dependent Protein Catabolic Process
Combined Score
OR
-log(q)
c
O G K
Ponceau
ROR2
HSP70
Ubiquitin
d
Ubiquitin
GFP-Ctrl-Normalized
OE
Ctrl
KD
e
HSP70
f
DMSO
MG132
OE GFP KD OE GFP KD
K48 Ubiquitin
Ponceau
g
K48 Ubiquitin
GFP-Ctrl- DMSO Normalized
DMSO
MG132
h
Proteasome Capacity
Proteasome Activity AUC
0 μM ATP
7 μM ATP
i
Puromycin Labeling Protein Synthesis
A.U.
j
35S-Met Labeling Protein Synthesis
m
Luciferase Refolding
GFP Control Normalized
k
Puromycin
GFP DMSO Normalized
l
Ubiquitin

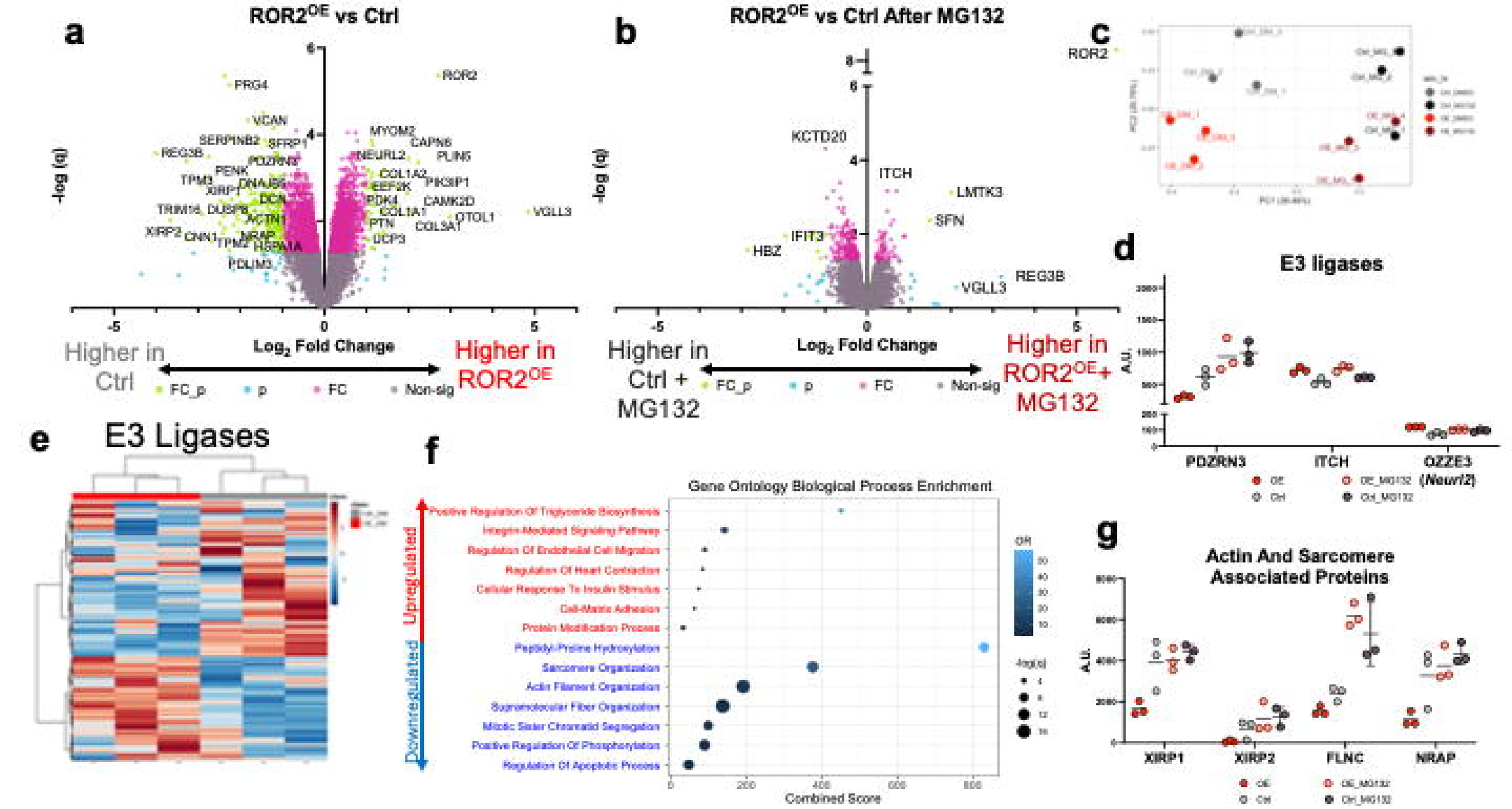
a
ROR2OE vs Ctrl
-log (p)
Log2 Fold Change
Higher in Ctrl
Higher in ROR2OE
FC_p
p
FC
Non-sig
ROR2
PRG4
VCAN
SERPINB2
SFRP1
REG3B
PDZRN3
PENK
TPM3
XIRP1
DNAJB6
DCN
TRIM16
DUSP6
ACTN1
XIRP2
CNN1
TPM2
NRAP
HSPA1A
PDLIM3
MYOM2
CAPN6
NEURL2
PLIN5
COL1A2
PIK3IP1
EEF2K
PDK4
CAMK2D
COL1A1
OTOL1
PTN
COL3A1
DCP3
VGLL3
b
ROR2OE vs Ctrl After MG132
KCTD20
ITCH
LMTK3
SFN
IFIT3
HBZ
VGLL3
REG3B
Higher in Ctrl + MG132
Higher in ROR2OE+ MG132
c
ROR2
d
E3 ligases
A.U.
PDZRN3
ITCH
OZZE3 (Neurl2)
OE
Ctrl
OE_MG132
Ctrl_MG132
e
E3 Ligases
f
Gene Ontology Biological Process Enrichment
Upregulated
Downregulated
Positive Regulation Of Triglyceride Biosynthesis
Integrin-Mediated Signaling Pathway
Regulation Of Endothelial Cell Migration
Regulation Of Heart Contraction
Cellular Response To Insulin Stimulus
Cell-Matrix Adhesion
Protein Modification Process
Peptidyl-Proline Hydroxylation
Sarcomere Organization
Actin Filament Organization
Supramolecular Fiber Organization
Mitotic Sister Chromatid Segregation
Positive Regulation Of Phosphorylation
Regulation Of Apoptotic Process
Combined Score
OR
-log(p)
g
Actin And Sarcomere Associated Proteins
A.U.
XIRP1
XIRP2
FLNC
NRAP
OE
Ctrl
OE_MG132
Ctrl_MG132

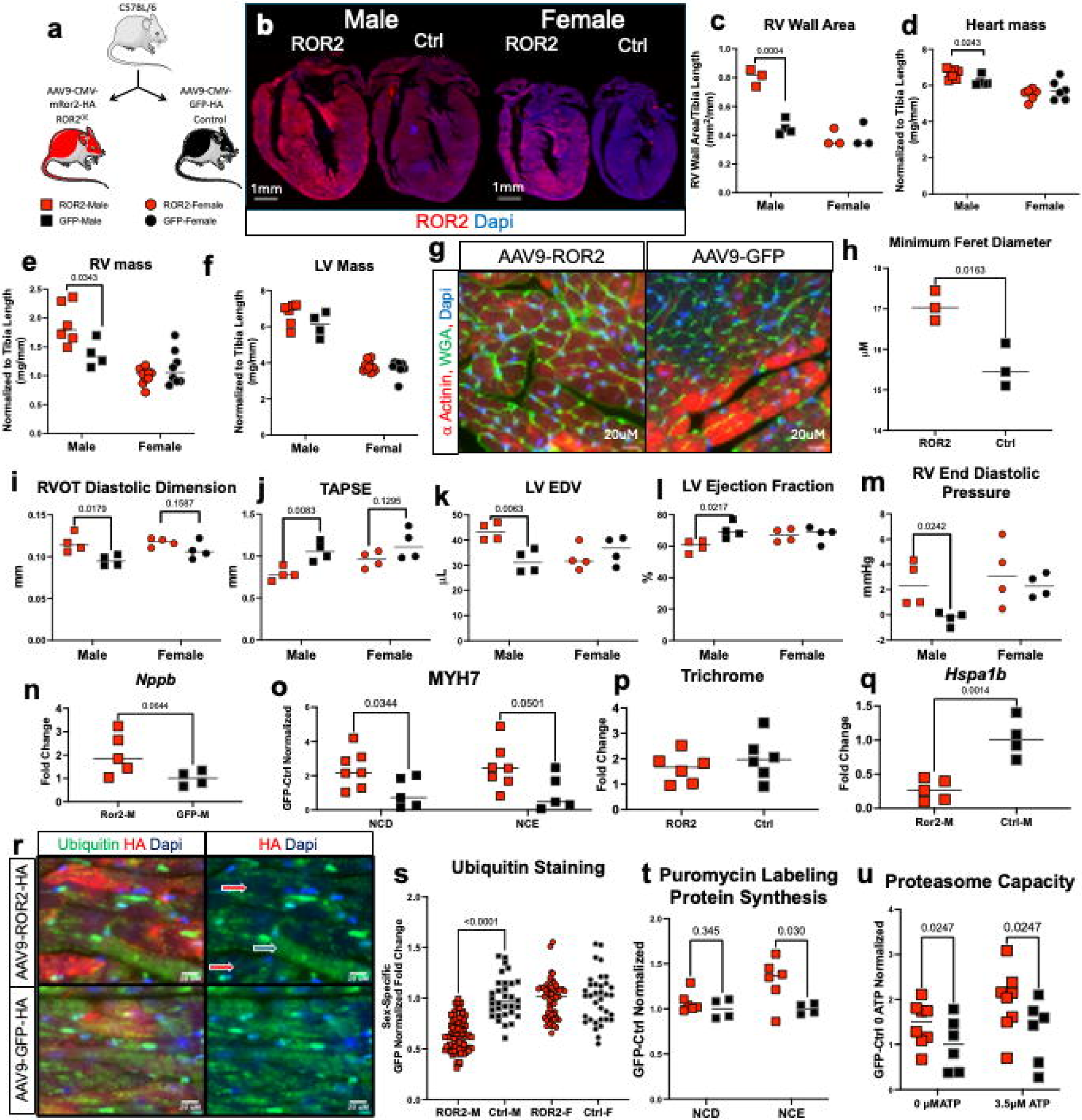
a
C57BL/6
AAV9-CMV-mRor2-HA
ROR2OE
AAV9-CMV-GFP-HA
Control
ROR2-Male
GFP-Male
ROR2-Female
GFP-Female
b
Male
Female
ROR2
Ctrl
ROR2
Ctrl
1mm
1mm
ROR2 Dapi
c
RV Wall Area
RV Wall Area/Tibia Length (mm²/mm)
0.0004
Male
Female
d
Heart mass
Normalized to Tibia Length (mg/mm)
0.0243
Male
Female
e
RV mass
Normalized to Tibia Length (mg/mm)
0.0343
Male
Female
f
LV Mass
Normalized to Tibia Length (mg/mm)
Male
Femal
g
AAV9-ROR2
AAV9-GFP
α Actinin, WGA, Dapi
20uM
20uM
h
Minimum Feret Diameter
μM
0.0163
ROR2
Ctrl
i
RVOT Diastolic Dimension
mm
0.0179
0.1587
Male
Female
j
TAPSE
mm
0.0083
0.1205
Male
Female
k
LV EDV
μL
0.0063
Male
Female
l
LV Ejection Fraction
%
0.0217
Male
Female
m
RV End Diastolic Pressure
mmHg
0.0242
Male
Female
n
Nppb
Fold Change
0.0044
Ror2-M
GFP-M
o
MYH7
GFP-Ctrl Normalized
0.0344
0.0501
NCD
NCE
p
Trichrome
Fold Change
ROR2
Ctrl
q
Hspa1b
Fold Change
0.0014
Ror2-M
Ctrl-M
r
Ubiquitin HA Dapi
HA Dapi
AAV9-ROR2-HA
AAV9-GFP-HA
s
Ubiquitin Staining
Sex-Specific GFP Normalized Fold Change
<0.0001
ROR2-M
Ctrl-M
ROR2-F
Ctrl-F
t
Puromycin Labeling Protein Synthesis
GFP-Ctrl Normalized
0.345
0.030
NCD
NCE
u
Proteasome Capacity
GFP-Ctrl 0 ATP Normalized
0.0247
0.0247
0 μMATP
3.5μM ATP

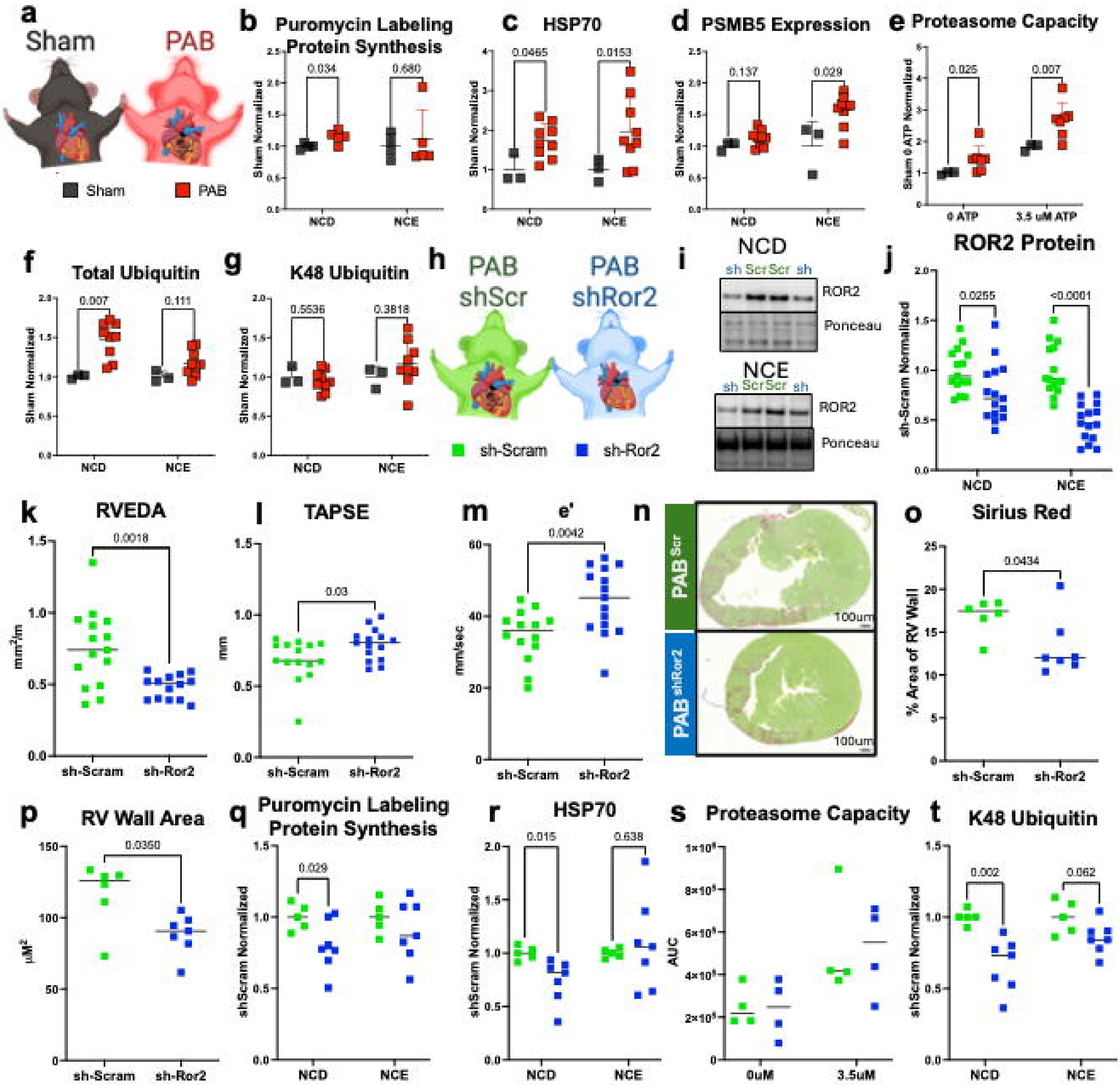
a
Sham
PAB
Sham
PAB
b Puromycin Labeling Protein Synthesis
Sham Normalized
0.034
0.680
NCD
NCE
c HSP70
0.0465
0.0153
d PSMB5 Expression
0.137
0.029
e Proteasome Capacity
Sham 0 ATP Normalized
0.026
0.007
0 ATP
3.5 uM ATP
f Total Ubiquitin
0.007
0.111
g K48 Ubiquitin
0.5536
0.3818
h
PAB shScr
PAB shRor2
sh-Scram
sh-Ror2
i
NCD
sh Scr Scr sh
ROR2
Ponceau
NCE
sh Scr Scr sh
ROR2
Ponceau
j ROR2 Protein
sh-Scram Normalized
0.0255
<0.0001
k RVEDA
mm²/m
0.0018
l TAPSE
mm
0.03
m e'
mm/sec
0.0042
n
PAB Scr
PAB shRor2
100um
100um
o Sirius Red
% Area of RV Wall
0.0434
sh-Scram
sh-Ror2
p RV Wall Area
μM²
0.0360
q Puromycin Labeling Protein Synthesis
shScram Normalized
0.029
r HSP70
shScram Normalized
0.015
0.638
s Proteasome Capacity
AUC
0uM
3.5uM
t K48 Ubiquitin
shScram Normalized
0.002
0.062

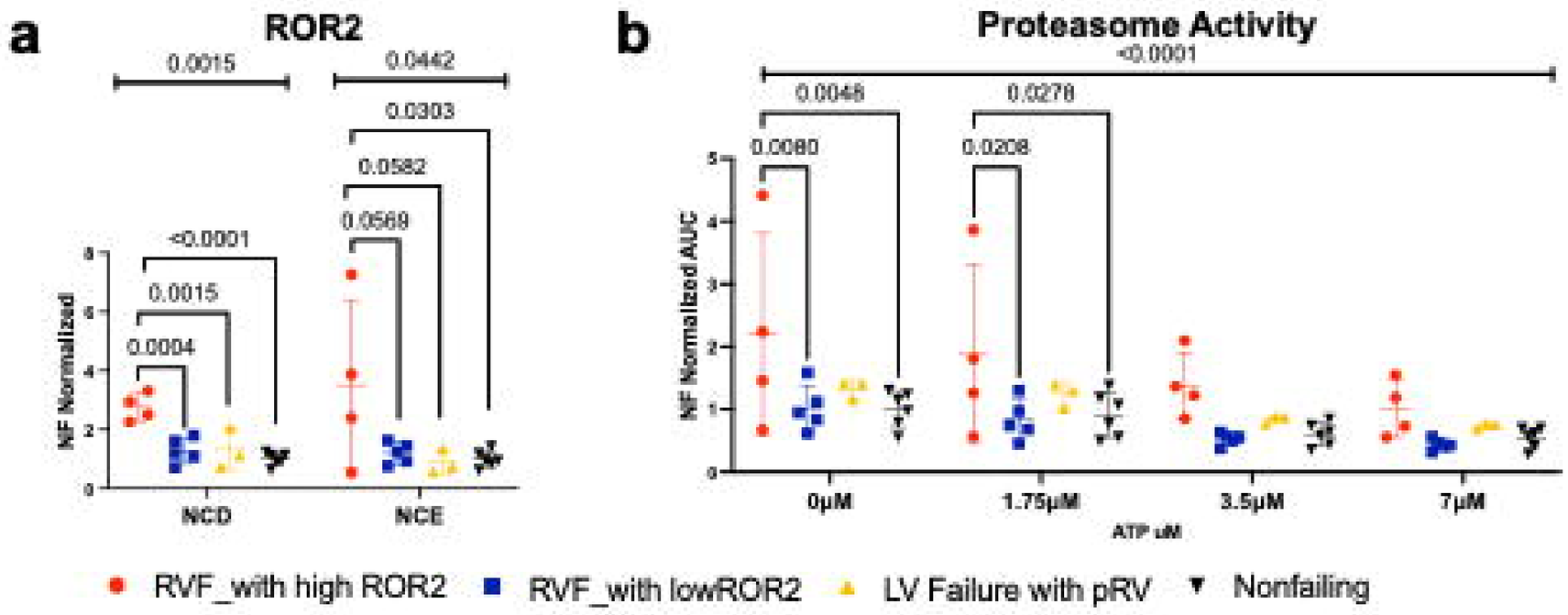
a
ROR2
0.0015
0.0442
0.0303
0.0582
0.0569
<0.0001
0.0015
0.0004
NF Normalized
NCD
NCE
b
Proteasome Activity
<0.0001
0.0046
0.0278
0.0080
0.0208
NF Normalized AUC
0μM
1.75μM
3.5μM
7μM
ATP uM
RVF_with high ROR2
RVF_with lowROR2
LV Failure with pRV
Nonfailing

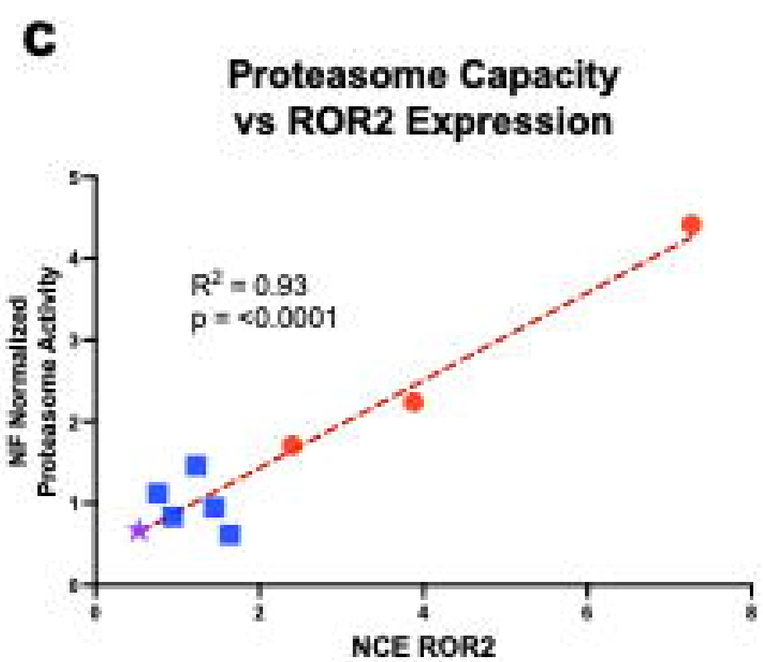
c
Proteasome Capacity
vs ROR2 Expression
R^2 = 0.93
p = <0.0001
NF Normalized
Proteasome Activity
NCE ROR2

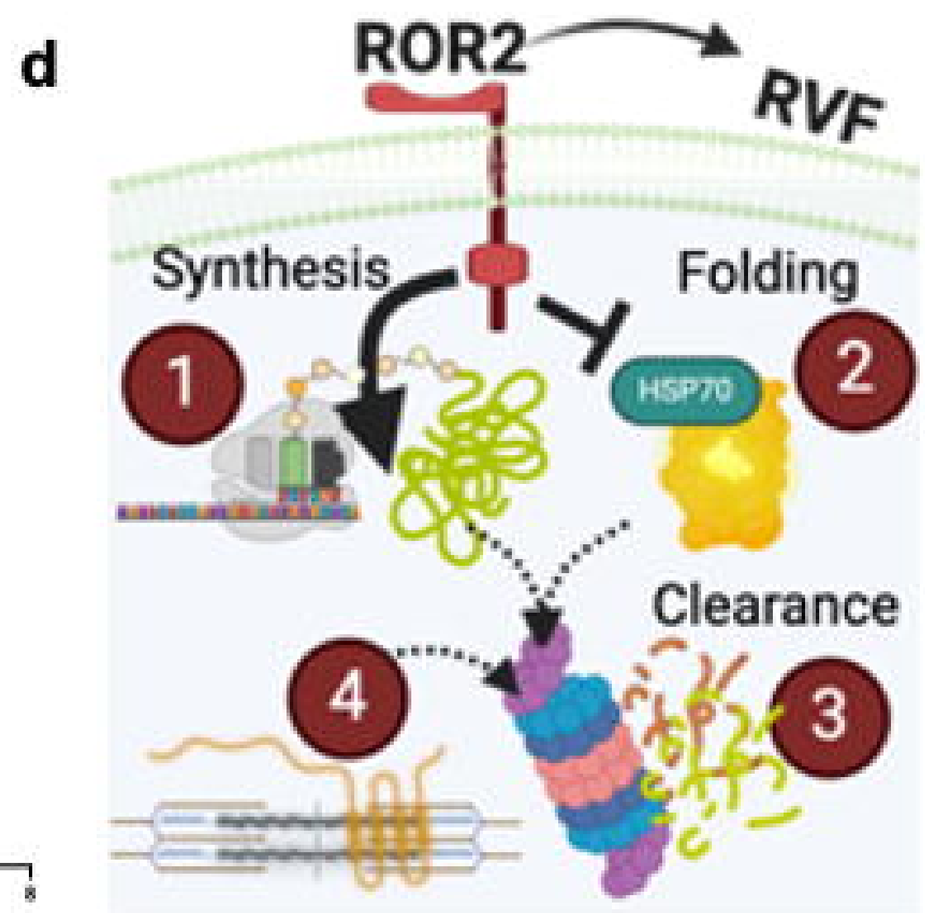
d
ROR2
RVF
Synthesis
Folding
HSP70
Clearance
1
2
3
4